nature plants

Article

https://doi.org/10.1038/s41477-025-02077-8

Vacuolar sorting receptors coordinate lytic vacuolar and autophagic transport for plant effector-triggered immunity

Received: 15 August 2024

Accepted: 10 July 2025

Published online: 18 August 2025

Check for updates

Dongmei Zhu[1,2,7], Shuai Hu[1,2,7], Wenhan Cao[1,2], Yanli Gao[1,2], Yan Li[1,2], Juan Xu[3], Baiying Li[4], Liwen Jiang[5], Enrique Rojo[6] & Jinbo Shen[1,2]

Vacuolar sorting receptors (VSRs) are involved in sorting soluble vacuolar proteins during normal plant growth and development, but their role in plant stress responses remains largely unexplored. Here we report that a subgroup of the *Arabidopsis thaliana VSR* genes are transcriptionally induced during infection with avirulent *Pseudomonas syringae* strains, leading to higher VSR protein accumulation. We demonstrate that the pathogen-responsive *VSR1*, *VSR5*, *VSR6* and *VSR7* genes function redundantly in sorting vacuolar death-related enzymes induced during bacterial infection. Moreover, VSRs are required for fusion of the tonoplast with the plasma membrane and the subsequent release of vacuolar contents into the apoplast, where bacterial pathogens reside. Indeed, dysfunction of this subgroup of *VSRs* blocks hypersensitive cell death and leads to stronger disease symptoms and higher bacterial loads, revealing their essential role in defence against avirulent bacterial infection. Intriguingly, their disruption also leads to defects in autophagy, impairing autophagosome-mediated degradation of bacterial effector proteins. Collectively, our results show that VSR1, VSR5, VSR6 and VSR7 are key regulators of plant effector-triggered immunity (ETI) by orchestrating receptor-mediated vacuolar sorting of immunity-related proteins, tonoplast to plasma membrane fusion, and autophagic degradation of effector proteins.

The lytic vacuole (LV) is the largest organelle in most vegetative plant cells and plays diverse roles at different stages of plant growth and development. The vacuole generates turgor pressure along with the cell wall to drive plant growth[1], and also influences the growth and fertilization processes of pollen tubes[2]. Furthermore, the vacuole plays a crucial role in cellular stress responses and various life activities, contributing substantially to plant growth and defence against environmental stress[3,4].

Soluble proteins are primarily transported into the vacuole via the secretory pathway in plants[5]. The sorting of these proteins occurs in the *trans*-Golgi network (TGN)/early endosome (EE), where the vacuolar sorting receptors (VSRs) play a crucial role in this sorting process. Soluble proteins containing vacuolar sorting signals, also known as cargo proteins, are recognized by VSRs in the TGN/EE and then transported into the prevacuolar compartment/multivesicular body (PVC/MVB), whereas those devoid of vacuolar sorting signals

[1]National Key Laboratory for Development and Utilization of Forest Food Resources, Zhejiang A&F University, Hangzhou, China. [2]Provincial Key Laboratory for Non-wood Forest and Quality Control and Utilization of Its Products, Zhejiang A&F University, Hangzhou, China. [3]State Key Laboratory of Plant Physiology and Biochemistry, College of Life Sciences, Zhejiang University, Hangzhou, China. [4]Department of Biology, Hong Kong Baptist University, Hong Kong, China. [5]Centre for Cell and Developmental Biology and State Key Laboratory of Agrobiotechnology, School of Life Sciences, The Chinese University of Hong Kong, Hong Kong, China. [6]Centro Nacional de Biotecnología, Consejo Superior de Investigaciones Científicas, Madrid, Spain. [7]These authors contributed equally: Dongmei Zhu, Shuai Hu. e-mail: jshen@zafu.edu.cn

are transported through the secretion pathway to the extracellular space[6,7]. Subsequently, the VSRs are recycled back to the TGN/EE by the retromer complex for further rounds of cargo binding, while the cargo proteins are ultimately sorted into the vacuoles. However, an emerging alternative model for cargo protein sorting and receptor recycling suggests that receptor–cargo sorting could initiate in the endoplasmic reticulum (ER) or the *cis*-Golgi, and the receptors dissociate from the cargo in the TGN, after which the VSRs would be transported back to the ER[8–11]. Despite the contending issues[12], both models coincide in the critical role that VSRs play in the sorting of vacuolar proteins. VSRs are a type-I transmembrane protein that contain an N-terminal domain (NT) to recognize soluble cargo in the lumen of endomembrane compartments and a C-terminal cytoplasmic tail (CT) to interact with cytosolic membrane trafficking factors for its correct targeting[13,14]. Several genetic assays have been employed to screen the machineries regulating VSR and soluble protein vacuolar trafficking in plants[15,16], with new regulators and unique mechanisms identified to be involved in regulating the subcellular distribution of VSRs and the delivery of VSR-dependent cargo into the vacuole[17–19].

Plant vacuolar proteins play important roles in the immune response to pathogen infection[20]. Under normal growth conditions, most vacuolar proteins are synthesized in the ER as precursor proteins and transported to the vacuole. Upon pathogen invasion, some precursor proteins can be cleaved and activated by vacuolar processing enzymes (VPE) to form active mature proteins, enabling a rapid immune response to pathogens[21]. Hydrolytic enzymes, including aspartate proteinases, cysteine proteinases and nucleases play a crucial role in the non-selective degradation of cellular components during programmed cell death (PCD), while defence proteins such as pathogenesis-related proteins (PR proteins), myrosinases, toxic proteins and lectins are required for defending against invading pathogens[20,22]. During incompatible infections with avirulent bacteria, vacuoles fuse with the plasma membrane (PM), leading to the release of antimicrobial proteinases and cell death inducers into the apoplast. This process is part of the hypersensitive response, ultimately resulting in cell death, preventing bacterial proliferation and halting the further spread of the disease[23,24]. While extensive efforts have been made to identify vacuole-localized proteins through vacuole isolation for mass spectrometry (MS) analysis[25], the specific sorting of these proteins by the VSR-mediated pathway and the regulatory mechanisms involved remain to be elucidated.

Type-III effector (T3E) proteins from plant pathogenic bacteria are delivered into the host cell where they manipulate host defence responses to benefit the pathogen[26]. Recent studies have demonstrated that microbial effectors perturb or hijack degradation machineries to attenuate plant immune responses[27,28]. The involvement of autophagy in plant–bacteria interactions is supported by evidence showing that certain effectors can employ distinct molecular strategies to enhance or suppress autophagy[29]. In addition, plant NEIGHBOUR OF BRCA1 gene 1 (NBR1), similar to its role in mammals, is involved in autophagy by degrading viral proteins[30]. Given that plant effectors are present intracellularly, it remains unclear how autophagy plays a role in plant–microbe interactions by targeting intracellular effectors.

Arabidopsis VSR1, VSR3 and VSR4 are involved in the vacuolar sorting of lytic enzymes in vegetative tissues, as well as storage proteins such as 12S globulins and 2S albumins in seeds[31]. Notably, recent studies have unveiled a novel function of VSR1 in osmotic stress tolerance and its role as a regulator in the synthesis of ABA, a crucial phytohormone involved in abiotic stress responses[32]. The *Arabidopsis* VSR family comprises seven protein members; the functional diversification within the VSR family is probably attributed to distinct expression patterns and sorting activities of the family members. Intriguingly, it was reported that *VSR6* and *VSR7* are primary targets for direct transcriptional induction by the key defence regulator NPR1 (ref. 33). Furthermore, recent experiments have identified a range of VSR-interacting vacuolar proteins related to plant disease resistance, including cysteine proteinase (CP) and its inhibitor (cysteine proteinase inhibitor, CPI)[14]. Thus, we hypothesized that *VSRs* responding to infection are likely to function in defence against pathogens.

In this study, we show that the pathogen-responsive *VSR1*, *VSR5*, *VSR6* and *VSR7* genes play relevant defensive functions as part of the plant effector-triggered immunity (ETI) against avirulent strains of *Pseudomonas syringae*. The deficiency in this subgroup of *VSRs* abolished vacuolar transport of immunity-related hydrolytic enzymes, disrupted the fusion between the tonoplast and the PM, blocked hypersensitive cell death and increased susceptibility to bacterial infection. Finally, we provide evidence that disruption of these *VSRs* affects autophagy and impairs the autophagic degradation of bacterial effector proteins. Our results provide valuable insights into the role of VSR-dependent vacuolar protein sorting and effector protein autophagic degradation in ETI.

Results

A subgroup of *VSR* genes is activated during infection with *P. syringae*

Transcript levels of *Arabidopsis VSR6* and *VSR7* are induced when NPR1 translocates into the nucleus in the absence of de novo protein synthesis[33], suggesting that they are direct transcriptional targets of this key immune regulator, which perceives salicylic acid generated

Fig. 1 | VSRs are induced and vacuolar enzymes of PLCPs are their cargo proteins in immune response. a, VSR proteins are upregulated after bacterial inoculation. Two-week-old seedlings of WT after inoculation with avirulent strains of *Pto* DC3000 expressing *avrRpm1*, *avrRpt2* or *avrRps4* (OD_{600} = 0.02) at the indicated time points (0 h, 3 h, 6 h and 12 h) were subjected to protein extraction and immunoblotting with anti-VSR antibodies. Anti-actin was used as a loading control (Source data). **b**, Quantification of the VSR protein levels in **a**. Immunoblot intensity was normalized to the loading control anti-actin, and the first lane (0 h) in each experiment was arbitrarily set to 1. Data are presented as means ± s.d. of three independent experiments (Source data). Different letters above bars indicate significant differences at $P < 0.05$ based on one-way ANOVA with Fisher's least significant difference (LSD) multiple comparisons test. **c**, Confocal images of cotyledon cells from Arabidopsis seedlings of the indicated genotypes transiently transformed with RD21B-mRFP, RDL2-mRFP, XCP1-mRFP, XBCP3-mRFP, RD19A-mRFP and CTB2-mRFP. Note that in the *vsr5vsr6vsr7* and *vsr1vsr6vsr7* triple mutants, reduced fluorescence signal in lytic vacuoles (asterisks) corresponded with much stronger signal in the extracellular space (arrows) compared with that in WT. Scale bars, 10 µm. **d**, Quantification of relative extracellular (EC) to intracellular (IC) fluorescence intensity values. The region of interest (ROI) was kept constant for each measurement. Data are presented as means ± s.d. of ten cells from three independent experiments. Different letters above bars indicate significant differences at $P < 0.05$, determined using one-way ANOVA with Fisher's LSD multiple comparisons test. **e**, Left: FRET analysis of the co-localized signal between Cerulean-VSR1 and YFP-tagged proteins RD21B, RDL2, XCP1, XBCP3, RD19A and CTB2. Aleurain-YFP and secYFP were used as positive and negative controls, respectively. The dominant negative mutant forms of AtSar1(H74L) were co-expressed to cause the relocalization of VSR and putative cargo proteins to the ER. Scale bar, 10 µm. Right: FRET efficiency was quantified using the AB approach. For each group, seven individual protoplasts were used for FRET efficiency quantification and statistical analysis. Data are presented as means ± s.d. of FRET efficiency. **f**–**h**, Co-IP analysis shows interaction between VSR1NT and putative cargo proteins. Soluble proteins were isolated from Arabidopsis protoplasts co-expressing truncated VSR1NT-Myc with individual YFP-tagged proteins RD21B, CTB2 (**f**), RDL2, RD19A (**g**), XCP1 or XBCP3 (**h**), followed by immunoprecipitation (IP) using GFP-Trap agarose beads and subsequent immunoblot analysis on eluted proteins using anti-GFP or anti-Myc antibodies. Aleurain-YFP and secYFP were respectively used as positive and negative controls for co-IP. The co-IP experiments (**f**–**h**) were repeated independently twice with similar results. Exact *P* values of statistical tests (**b**, **d** and **e**) are provided as Source data.

https://doi.org/10.1038/s41477-025-02077-8

during infection and confers broad-spectrum resistance against bacterial, fungal and viral pathogens in many plant species[34]. We decided to focus on the *Arabidopsis thaliana*–*P. syringae* model pathosystem, which involves NPR1-dependent immunity[35]. Analysis of microarray datasets revealed that *VSR* genes exhibit high expression across various cell types within leaf tissues (Supplementary Fig. 1a), and the expression of *VSR6* and *VSR7* is induced after infection of *A. thaliana* (hereafter, Arabidopsis) with different *P. syringae* strains (Supplementary Fig. 1b), suggesting that they could be part of an NPR1-triggered defence response and may have a role in protection against this pathogen.

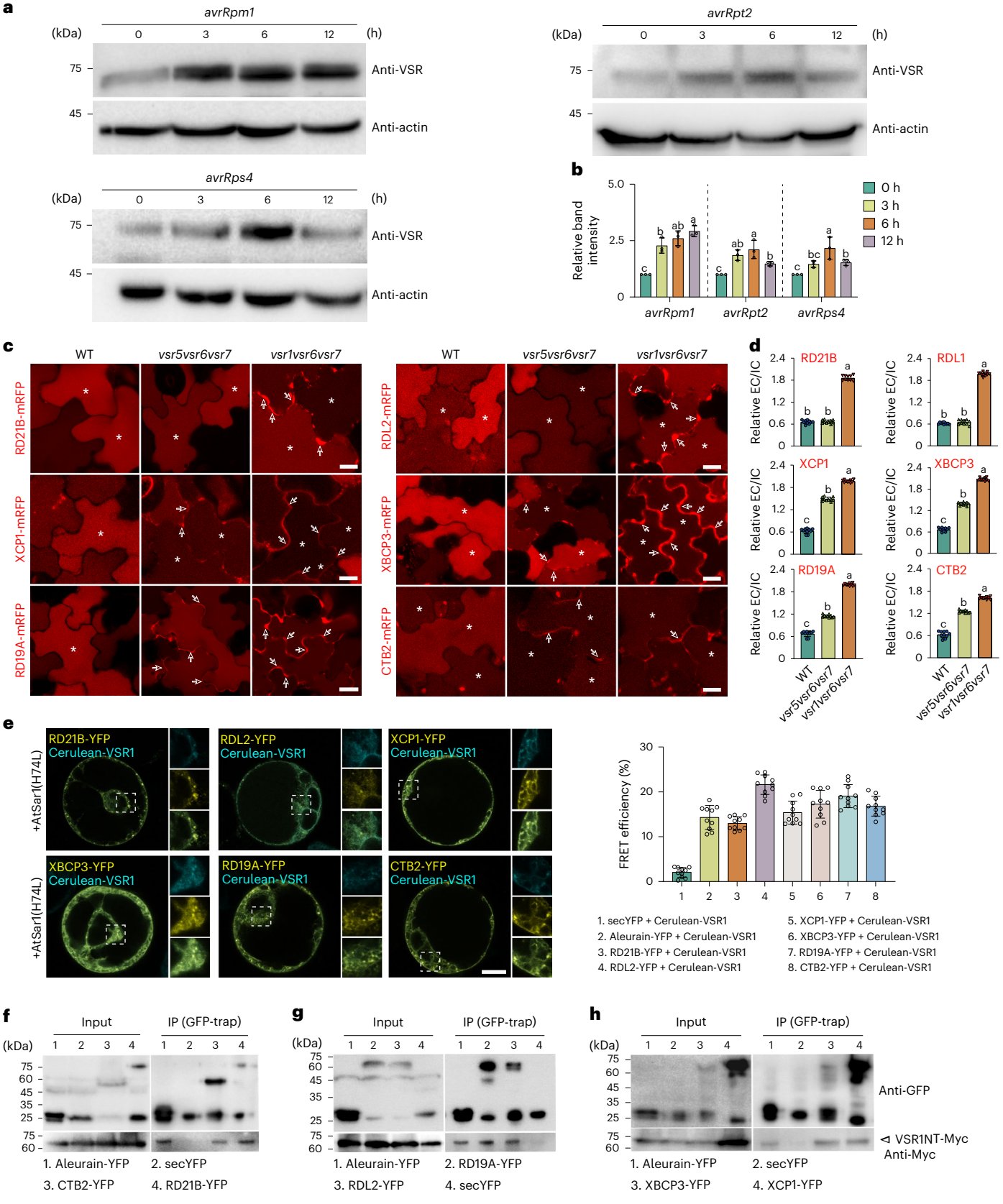

To confirm that VSRs are induced after infection with *P. syringae*, we examined the changes in VSR protein levels by immunoblot assays in time-course experiments. Twelve-day-old wild-type (WT) seedlings grown in liquid medium were inoculated with avirulent strains of *Pto* DC3000 harbouring *avrRpm1*, *avrRpt2* or *avrRps4*, followed by protein extraction and immunoblot assays using anti-VSR antibody (Fig. 1a). The VSR antibody was raised against the N-terminal ligand binding domain of the Arabidopsis VSR1 recombinant protein and can detect Arabidopsis VSR homologues[36]. Relative quantitative analysis by immunoblot assays showed that the VSR protein levels increased within 3–6 h after inoculation with the different strains (Fig. 1b). Consistent with increased VSR protein accumulation, quantitative PCR with reverse transcription (RT–qPCR) analysis of each *VSR* transcript showed that increased transcript levels of *VSR1*, *VSR4*, *VSR5*, *VSR6* and *VSR7* could be detected after 3 h of incubation with *Pto* DC3000 expressing *avrRpm1*, *avrRpt2* or *avrRps4* in both seedlings and mature leaves, although the degree of induction varied for each strain (Supplementary Fig. 1c–h). Taken together, these results suggest that VSR proteins are upregulated in response to bacterial effectors, indicating their potential involvement in plant immune responses.

To assess the role of VSRs in the interaction with *P. syringae*, we concentrated on the transcriptionally responsive genes (*VSR1*, *VSR4*, *VSR5*, *VSR6* and *VSR7*) and generated multiple mutant combinations. We first established the *vsr6vsr7* double mutant from our previously obtained T-DNA insertional alleles[31]. The *vsr6vsr7* mutant had no obvious phenotype compared with WT controls when plants were germinated and grown under either long-day or short-day conditions (Extended Data Fig. 1a–c). The mutant *vsr6vsr7* was then crossed with homozygous *vsr1*, *vsr4* or *vsr5*. Using PCR-based genotyping, we isolated *vsr5vsr6vsr7* seedlings, which had normal germination and growth (Extended Data Fig. 1a–c). In contrast, the *vsr1vsr6vsr7* had smaller rosette size but similar root growth compared with WT. Expression of GFP-VSR1 under the control of the native promoter (*VSR1pro::GFP-gVSR1*) complemented the *vsr1vsr6vsr7* rosette growth phenotype, thus confirming that it was due to *VSR* dysfunction and suggesting that the chimaeric protein is functional in plants. The *vsr4*(+/−)*vsr6vsr7* plant also showed smaller rosettes and shorter roots ($P < 0.05$) than WT (Extended Data Fig. 1a–c). Moreover, in an F3 population derived from the self-pollination of *vsr4*(+/−)*vsr6vsr7* plants, we did not recover homozygous *vsr4vsr6vsr7* triple mutant plants, suggesting that loss of function of these three *VSR* genes is lethal. Therefore, in the following experiments, we focused on the viable *vsr5vsr6vsr7* and *vsr1vsr6vsr7* triple mutants to investigate the function of VSRs during immune responses. In addition, we generated transgenic lines expressing *VSR1pro::GFP-gVSR1*, *VSR5pro::GFP-gVSR5*, *VSR6pro::GFP-gVSR6* and *VSR7pro::GFP-gVSR7* under the control of their native promoters. Confocal microscopy demonstrated that the promoters are active in leaves, including both mesophyll and epidermal cells (Supplementary Fig. 2a–d). Moreover, the GFP-tagged VSR proteins localized to distinct punctate structures, consistent with their known association with the PVC/MVB[37,38]. Therefore, in subsequent experiments, we focused on characterizing the functional roles of *VSR1*, *VSR5*, *VSR6* and *VSR7* during immune responses after leaf infection with *P. syringae*.

Identification of pathogen-induced vacuolar enzymes as VSR cargo proteins

In the plant endomembrane system, VSRs bind cargo proteins and facilitate their transport to the vacuole. Moreover, vacuolar enzymes are known to play a role in cell death and immunity to pathogen infection[20,39,40]. To identify VSR cargo potentially involved in plant immunity, we conducted time-course transcriptome analysis of WT plants inoculated with virulent and avirulent *P. syringae* strains to detect global alterations in gene transcription. This led to the identification of genes whose transcript levels increased after infection and met the criteria for VSR cargo, that is, soluble protein containing signal peptide (Supplementary Table 1). The list of candidates was further filtered out by searching for their presence in previously published vacuolar protein or VSR cargo datasets[14,25]. In total, we identified 19 upregulated genes as putative VSR vacuolar cargo with potential roles in the defence response to *P. syringae* infection (Extended Data Fig. 2a), including 11 papain-like cysteine proteases (PLCPs) (RD21A, RD21B, RDL1, RDL2, XCP1, XBCP3, PAP1, RD19A, RD19B, AALP and CTB2), 3 vacuolar peroxidases (PRX33, PRX34 and PRX37), 2 pathogenesis-related (PR) proteins with endochitinase activity (PR3 and PR4), a carboxypeptidase (CPY), an aspartyl-protease A1 homologous to yeast PEP4 homology (PEP4) and the redox enzyme glutaredoxin (GRX). Out of the 19 identified proteins, only the aleurain-like protease (AALP) and GRX had been previously described as VSR-interacting proteins[14,41].

VSR-mediated cargo proteins are known to traffic through PVCs/MVBs before reaching vacuoles in plant cells[42]. Therefore, we tested the PVC/MVB localization of the putative cargo proteins by co-localization with VSR marker proteins. As a positive control, aleurain-GFP (GFP with signal peptide and a vacuolar sorting determinant)[14,43] showed co-localization in punctate structures with the PVC/MVB marker mRFP-VSR2 as well as a diffuse pattern in the vacuole, while the secreted protein secYFP (YFP with signal peptide), exhibited a typical ER pattern without fluorescence in the vacuole (Extended Data Fig. 2b). The remaining 19 putative cargo proteins fused to GFP/YFP (note that for proteins containing potential C-terminal vacuolar sorting signals, signal peptide-GFP/YFP was fused at the N terminus) also showed punctae fluorescence co-localizing with the PVC/MVB marker mRFP-VSR2 and a diffuse fluorescence pattern corresponding to the vacuole (Extended Data Fig. 2c,d), suggesting that they are transported to the vacuole via the PVC/MVB.

When VSR is mutated, the cargo is abnormally secreted into the extracellular spaces[15,31,44]. To assay whether the newly identified proteins are indeed VSR cargo, we examined the trafficking of mRFP-labelled versions in vegetative tissues of WT and *vsr* mutant plants. Consistent with their subcellular localization in the protoplasts, all 19 mRFP-tagged proteins tested uniformly labelled the cell interior, occupied almost entirely by the vacuole, in cotyledon epidermal cells of WT plants (Fig. 1c and Extended Data Fig. 3a). In contrast, we observed partial secretion of several proteins in *vsr5vsr6vsr7* plants, with mRFP labelling the extracellular space (ECS). Moreover, in the *vsr1vsr6vsr7* mutant, all cargo proteins tested were partially secreted into the ECS and showed reduced vacuolar levels relative to WT or *vsr5vsr6vsr7* plants (Fig. 1d and Extended Data Fig. 3b). This suggests that the *vsr1vsr6vsr7* mutant has more severe defects in protein trafficking to the vacuole in vegetative tissues. VPEγ is a vacuolar-localized caspase-like protease involved in cell death progression during the hypersensitive response in pathogen defence[39]. VPEγ is targeted to the vacuole through a specific pathway involving ER-derived vesicles[45,46]. In WT plants, VPEγ-mRFP labelled the vacuole in cotyledon epidermal cells, but it was not secreted in *vsr5vsr6vsr7* or *vsr1vsr6vsr7* mutants (Extended Data Fig. 3a,b), thereby highlighting the potential specificity of VSRs for sorting particular pathogen-induced vacuolar proteins. Taken together, these results support the conclusion that the identified pathogen-induced proteins are VSR cargo.

To confirm that they are bonafide VSR cargo, we focused on PLCPs, which have been associated with immunity and senescence[47,48]. We selected six PLCPs and tested their interaction with VSR by multiple approaches. We first constructed acceptor photobleaching–fluorescence resonance energy transfer (FRET–AB) assays in protoplasts. We co-expressed cerulean-VSR1 and YFP-tagged cargo proteins together with a dominant negative mutant version of Arabidopsis Sar1 GTPase (AtSar1 H74L), which inhibits ER-Golgi transport and retains VSRs and soluble proteins in the ER[49,50], where VSR-cargo binding can be measured[8,51]. Indeed, cerulean-VSR1 and the YFP-tagged putative cargo proteins were co-localized at tubular ER structures when co-expressed with AtSar1 H74L (Fig. 1e). Moreover, FRET–AB analysis

https://doi.org/10.1038/s41477-025-02077-8

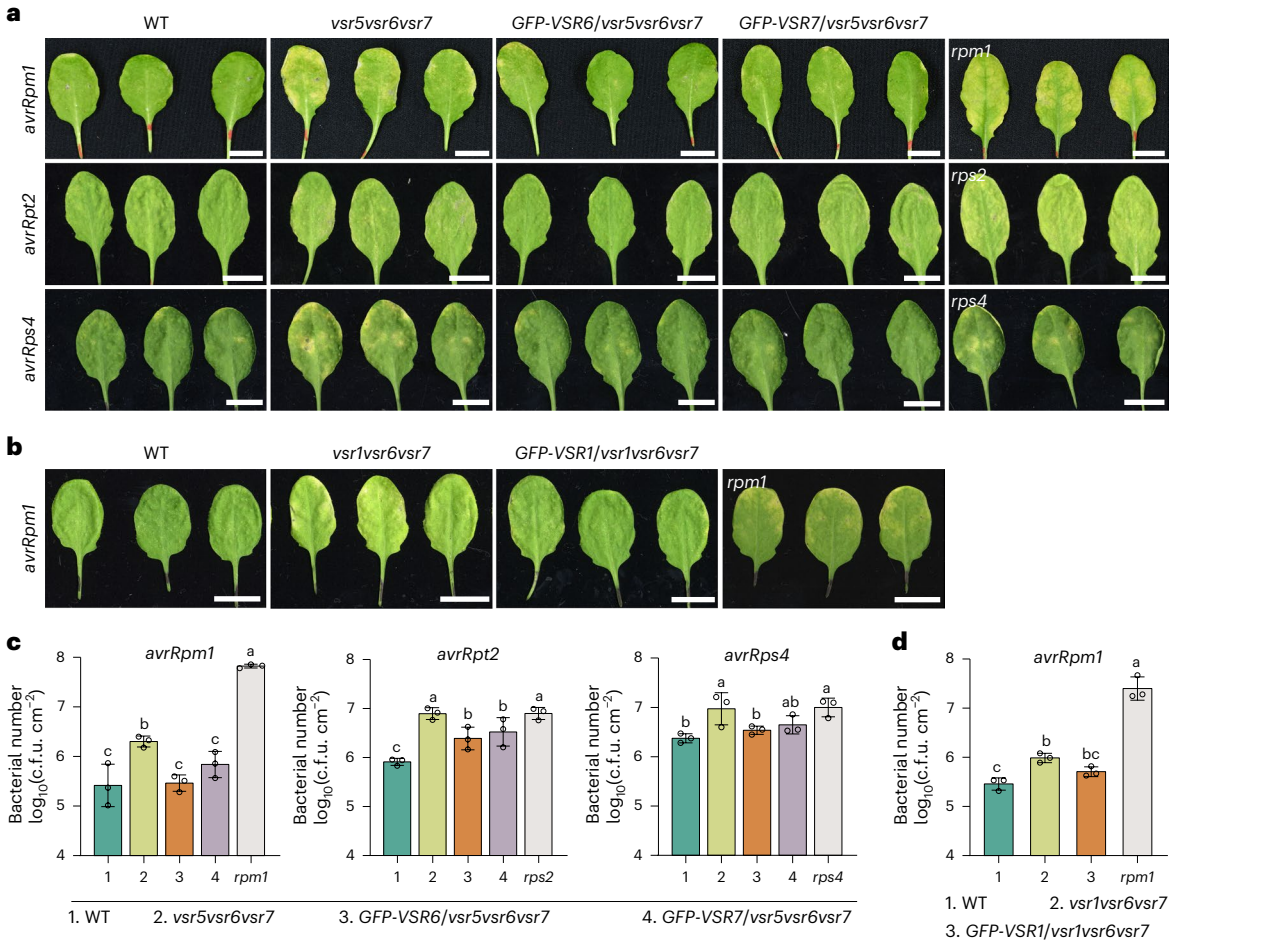

Fig. 2 | VSR proteins are required for ETI process. a, Disease symptoms on representative infected leaves were monitored 3 days after inoculation. Leaves were of WT, *vsr5vsr6vsr7* triple mutant, and complemented line *GFP-VSR6/vsr5vsr6vsr7* or *GFP-VSR7/vsr5vsr6vsr7* after 3 days inoculation with the *Pto* DC3000 expressing *avrRpm1* (OD_{600} = 0.001), *avrRpt2* (OD_{600} = 0.001) or *avrRps4* (OD_{600} = 0.005). The *vsr5vsr6vsr7* leaves inoculated with indicated avirulent bacterial strain exhibit more severe chlorotic symptoms than other genotypes. Loss-of-function mutants of the corresponding resistance genes *RPM1* (*rpm1*), *RPS2* (*rps2*) and *RPS4* (*rps4*) served as additional controls. Scale bars, 1 cm. **b**, Disease symptoms on representative infected leaves were monitored 3 days after inoculation. Leaves of WT, *vsr1vsr6vsr7* triple mutant and complemented line *GFP-VSR1/vsr1vsr6vsr7* after 3 days inoculation with *Pto* DC3000 *avrRpm1* (OD_{600} = 0.001). The inoculated *vsr1vsr6vsr7* and *rpm1* leaves exhibit chlorotic symptoms. Scale bars, 1 cm. **c**,**d**, Bacterial growth 3 days after inoculation with *Pto* DC3000 expressing *avrRpm1* (OD_{600} = 0.001), *avrRpt2* (OD_{600} = 0.001) or *avrRps4* (OD_{600} = 0.005) in the leaves of *vsr5vsr6vsr7* (**c**), *vsr1vsr6vsr7* (**d**), complemented lines or the corresponding resistance gene mutants. Each bar represents log_{10}-transformed values of the mean ± s.d. of three biological replicates. Experiments were repeated three times with similar results. Different letters above bars indicate significant differences at $P < 0.05$, determined using one-way ANOVA with Fisher's LSD multiple comparisons test. Exact *P* values are provided as Source data.

suggests that the putative cargos RD21B-YFP, RDL2-YFP, XCP1-YFP, XBCP3-YFP, RD19A-YFP and CTB2-YFP, but not control secYFP, interact with cerulean-VSR1 in the ER lumen of Arabidopsis protoplasts (Fig. 1e). To confirm these interactions, co-immunoprecipitation (co-IP) experiments were carried out in samples from protoplasts transiently co-expressing the N-terminal ligand binding domain of VSR fused to the Myc epitope (VSR1NT-Myc) and YFP-tagged cargo proteins. Proteins were purified using GFP-Trap beads and analysed by western blotting with anti-GFP or anti-Myc antibodies. secYFP was used as a negative control for the co-immunoprecipitation assays. As shown in Fig. 1f–h, VSR1NT-Myc co-immunopurified with aleurain-YFP, RD21B-YFP, RDL2-YFP, XCP1-YFP, XBCP3-YFP, RD19A-YFP and CTB2-YFP, but not with the control secYFP. These findings support the direct interaction of VSR1 with these PLCPs. Interestingly, in the western blot analysis of immunoprecipitates using anti-GFP antibodies, a large amount of a 28-kDa YFP core was detected, which is a hallmark of the markers reaching the vacuole[52,53]. In summary, the subcellular localization, FRET assays and co-IP experiments collectively suggest that these identified plant immunity-related PLCPs are cargo proteins for VSRs.

VSRs are required for ETI against *P. syringae*

Having established that a subgroup of *VSRs* is involved in sorting *P. syringae*-induced vacuolar enzymes, we next analysed their actual roles in the plant immune response against *P. syringae* infection. Inoculation of *Pto* DC3000 *avrRpm1* onto the *vsr5vsr6vsr7* or *vsr1vsr6vsr7* mutants resulted in increased disease symptoms relative to WT plants. The leaves of the triple mutants displayed large chlorotic areas at 3 days post inoculation (dpi), whereas leaves from WT plants remained relatively green and healthy (Fig. 2a,b). In addition, bacterial proliferation in the *vsr5vsr6vsr7* or *vsr1vsr6vsr7* plants was significantly increased ($P < 0.05$) relative to WT plants, although not to the levels observed in *rpm1* plants used as an immunocompromised control genotype (Fig. 2c,d). Furthermore, complementation lines carrying *VSR6pro::GFP-gVSR6* or *VSR7pro::GFP-gVSR7* in the *vsr5vsr6vsr7* background, as well as *VSR1pro::GFP-gVSR1* in the *vsr1vsr6vsr7* background, partially rescued the increased susceptibility to bacterial infection (Fig. 2a–d). To determine whether the requirement of VSRs for ETI is specific to *Pto* DC3000 *avrRpm1*, we examined the bacterial growth of two additional bacterial strains, *Pto* DC3000 carrying

avrRpt2 or *avrRps4*. Infection with the *Pto* DC3000 carrying *avrRpt2* or *avrRps4* also resulted in significantly ($P < 0.05$) increased bacterial growth on *vsr5vsr6vsr7* relative to that observed on WT plants (Fig. 2a,c). In addition, this effect was partially complemented in *GFP-VSR6/vsr5vsr6vsr7* or *GFP-VSR7/vsr5vsr6vsr7* plants. Thus, these results indicate that *VSR1*, *VSR5*, *VSR6* and *VSR7* are involved in RPM1-, RPS2- and PRS4-mediated ETI.

Interestingly, VSR protein levels were also increased after inoculation with the virulent strain *Pto* DC3000 EV (Extended Data Fig. 4a). In addition, slightly increased disease symptoms and bacterial growth of *Pto* DC3000 EV were observed in *vsr5vsr6vsr7* plants compared with WT plants (Extended Data Fig. 4b,c), suggesting that VSR proteins are also involved in PAMP-triggered immunity (PTI). However, the effects of *vsr5vsr6vsr7* deficiency on the increased bacterial growth of *Pto* DC3000 EV [2.97-fold increase in colony-forming units (c.f.u.) cm^{-2}] were much smaller than that of *Pto* DC3000 *avrRpm1* (7.66-fold increase), *Pto* DC3000 *avrRpt2* (9.67-fold increase) or *Pto* DC3000 *avrRps4* (3.96-fold increase), indicating that VSR proteins are probably weakly involved in PTI. To confirm this hypothesis, we inoculated WT, *vsr5vsr6vsr7* and *vsr1vsr6vsr7* plants with *Pto* DC3000 *hrcC*$^-$, which is defective in type-III secretion and activates PTI but not ETI in Arabidopsis[54]. The *vsr5vsr6vsr7* and *vsr1vsr6vsr7* plants did not exhibit a difference in growth of *Pto* DC3000 *hrcC*$^-$ compared with WT plants (Extended Data Fig. 4d,e). Moreover, *Pto* DC3000 *hrcC*$^-$ inoculation induced a similar number of highly localized callose deposits in the leaves of *vsr5vsr6vsr7* and *vsr1vsr6vsr7* plants compared with WT plants (Extended Data Fig. 4f). These results indicate that the VSR proteins are not required for induced callose deposition and support our conclusion that the VSRs are crucial for efficient ETI but only weakly involved in PTI.

VSR deficiency reduces hypersensitive cell death during ETI

ETI is often associated with hypersensitive cell death[55]. To determine whether *VSR* deficiency affects hypersensitive cell death, we first used trypan blue staining to monitor cell death in WT, *vsr5vsr6vsr7* and complemented *GFP-VSR6/vsr5vsr6vsr7* or *GFP-VSR7/vsr5vsr6vsr7* lines at 12 h post inoculation (hpi) with *Pto* DC3000 *avrRpm1*. The *vsr5vsr6vsr7* mutant had much fewer ($P < 0.001$) dead cells, distinctive as blue dots, per unit leaf area than WT plants (Fig. 3a) and had levels close to those of the *rpm1* mutant, which is blocked in avrRpm1-induced hypersensitive cell death. Moreover, in *GFP-VSR6/vsr5vsr6vsr7* or *GFP-VSR7/vsr5vsr6vsr7* plants, the hypersensitive cell death response was partially recovered to levels close to those observed in WT plants. A similar reduction in hypersensitive cell death measured by trypan blue staining was observed when the *vsr5vsr6vsr7* mutant was inoculated with *Pto* DC3000 *avrRpt2* or *Pto* DC3000 *avrRps4* (Fig. 3b–d), although *Pto* DC3000 *avrRps4*-induced hypersensitive cell death was relatively weak in Col-0 plants[56,57]. The reduction in hypersensitive cell death was also partially complemented in *GFP-VSR6/vsr5vsr6vsr7* and *GFP-VSR7/vsr5vsr6vsr7* plants. In addition, the *vsr1vsr6vsr7* mutant also contained much fewer numbers ($P < 0.001$) of dead cells after inoculation with *Pto* DC3000 *avrRpm1* than WT plants (Fig. 3e).

To confirm these results, hypersensitive cell death was also monitored by ion leakage assays, which measure conductance increases upon loss of membrane integrity in dying leaf tissue[58,59]. In WT, an increase in conductivity was already apparent at 4 hpi with *Pto* DC3000 *avrRpm1*, steadily increasing up to 12 hpi. The increase in conductivity was delayed in *vsr5vsr6vsr7* and *rpm1* plants, reaching significantly decreased levels ($P < 0.05$) at 12 hpi compared with WT (Fig. 3f). In addition, ion leakage in *GFP-VSR6/vsr5vsr6vsr7* or *GFP-VSR7/vsr5vsr6vsr7* lines was intermediate between *vsr5vsr6vsr7* and WT plants. Most strikingly, *vsr1vsr6vsr7* showed strong suppression of cell death as measured by ion leakage upon *Pto* DC3000 *avrRpm1* infection, while *GFP-VSR1/vsr1vsr6vsr7* showed almost complete complementation of this phenotype (Fig. 3g). In conclusion, these assays suggest that *VSR1*, *VSR5*, *VSR6* and *VSR7* positively regulate hypersensitive cell death induction during ETI.

To test whether the remaining *VSR* genes, *VSR2*, *VSR3* and *VSR4*, play a role in the plant immune response against *P. syringae* infection, we generated a *VSR3* and *VSR4* CRISPR knockout mutant in the *vsr2* T-DNA insertion mutant background, termed *vsr2VSR3*^{Cas9}*VSR4*^{Cas9}*-1* using the CRISPR-Cas9 system as described previously[60]. Genomic DNA sequencing of the *vsr2VSR3*^{Cas9}*VSR4*^{Cas9}*-1* line revealed an editing event spanning the first exon of both *VSR3* and *VSR4*, which introduced extrinsic amino acid residues and resulted in a premature stop codon (Extended Data Fig. 5a,b). The *vsr2VSR3*^{Cas9}*VSR4*^{Cas9}*-1* mutant had normal germination and growth under either long-day or short-day condition (Extended Data Fig. 5c,d). However, the inoculation of *Pto* DC3000 *avrRpm1* or *Pto* DC3000 EV onto the *vsr2VSR3*^{Cas9}*VSR4*^{Cas9}*-1* mutant did not show obvious differences in disease symptoms or in bacterial growth relative to WT plants (Extended Data Fig. 5e–h), suggesting that *VSR2*, *VSR3* and *VSR4* may not be involved in resistance to the pathogens tested. Moreover, we used trypan blue staining to monitor cell death in WT, *vsr2VSR3*^{Cas9}*VSR4*^{Cas9}*-1* mutant and *rpm1* lines, at 12 hpi, with *Pto* DC3000 *avrRpm1*. The *vsr2VSR3*^{Cas9}*VSR4*^{Cas9}*-1* mutant had a similar number ($P > 0.05$) of dead cells as the WT plants (Extended Data Fig. 5i). Taken together, the obtained data suggest that *VSR2, VSR3* and *VSR4* genes do not play a substantial role in ETI responses to *P. syringae*.

VSRs are required for tonoplast fusion with the PM during ETI

Hypersensitive cell death in response to avirulent bacterial infection is associated with the fusion of the central vacuole with the PM[24]. The reduced cell death in response to avirulent bacterial infection in the triple *vsr* mutants prompted us to investigate membrane fusion between the vacuolar membrane and the PM. To observe membrane fusion in plants, we generated a transgenic plant expressing the tonoplast marker YFP-VAMP711 in WT, *vsr5vsr6vsr7* and *vsr1vsr6vsr7* mutants. The leaves of plants were inoculated with *Pto* DC3000 *avrRpm1* and then stained with FM4-64 for confocal microscopy immediately (0 h) or 3 h after inoculation. The fluorescences of the FM4-64-stained PM and the YFP-VAMP711-labelled tonoplast were separated in infected leaves immediately after inoculation (Fig. 4a). However, after 3 hpi with *Pto* DC3000 *avrRpm1*, the fluorescence of the FM4-64-stained PM and the YFP-VAMP711-labelled tonoplast co-localized and surrounded the chloroplasts in most WT cells from infected leaves (Fig. 4a), consistent with previous observations[24]. However, the frequencies of cells with co-localization between FM4-64 and YFP-VAMP711 were reduced in infected leaves of *vsr5vsr6vsr7* and *vsr1vsr6vsr7* plants. A statistical analysis showed that cells with tonoplast and PM fusion occurred in 80.9 ± 7.3% ($n = 40$) of the WT cells, compared with 48.1 ± 1.4% ($n = 40$) in *vsr5vsr6vsr7*, and 17.7 ± 1.5% ($n = 40$) in *vsr1vsr6vsr7* mutants examined at 3 hpi (Fig. 4b). These results indicate that VSR is required for membrane fusion between the tonoplast and the PM in response to *Pto* DC3000 *avrRpm1* infection.

The fusion of the PM and vacuole membrane causes the discharge of vacuolar proteins to the outside of the bacteria-infected cells. To observe vacuolar protein release into the ECS in infected leaves, we first generated WT, *vsr5vsr6vsr7* and *vsr1vsr6vsr7* plants stably expressing the vacuolar protein marker spL-RFP, consisting of RFP fused to the vacuolar sorting signal of proricin[61]. The fluorescence became detectable in the ECS of WT leaf mesophyll cells at 3.5 hpi with *Pto* DC3000 *avrRpm1* (Fig. 4c). However, the discharge into the ECS of the vacuolar marker was reduced ($P < 0.001$) in *vsr5vsr6vsr7* and *vsr1vsr6vsr7* infected cells at 3.5 or 4.5 hpi (Fig. 4d). To confirm the results, we used the pH-sensitive, membrane-permeable fluorescent dye 2′,7′-bis-(2-carboxyethyl)-5-(and-6)-carboxyfluorescein acetoxymethyl ester (BCECF-AM), which is loaded into vacuoles allowing visualization of their integrity[62]. Staining results showed that in WT plants, BCECF-AM fluorescence was maintained in the vacuole at 0 hpi and became gradually detectable in the ECS at 3.5 hpi (Fig. 4e).

https://doi.org/10.1038/s41477-025-02077-8

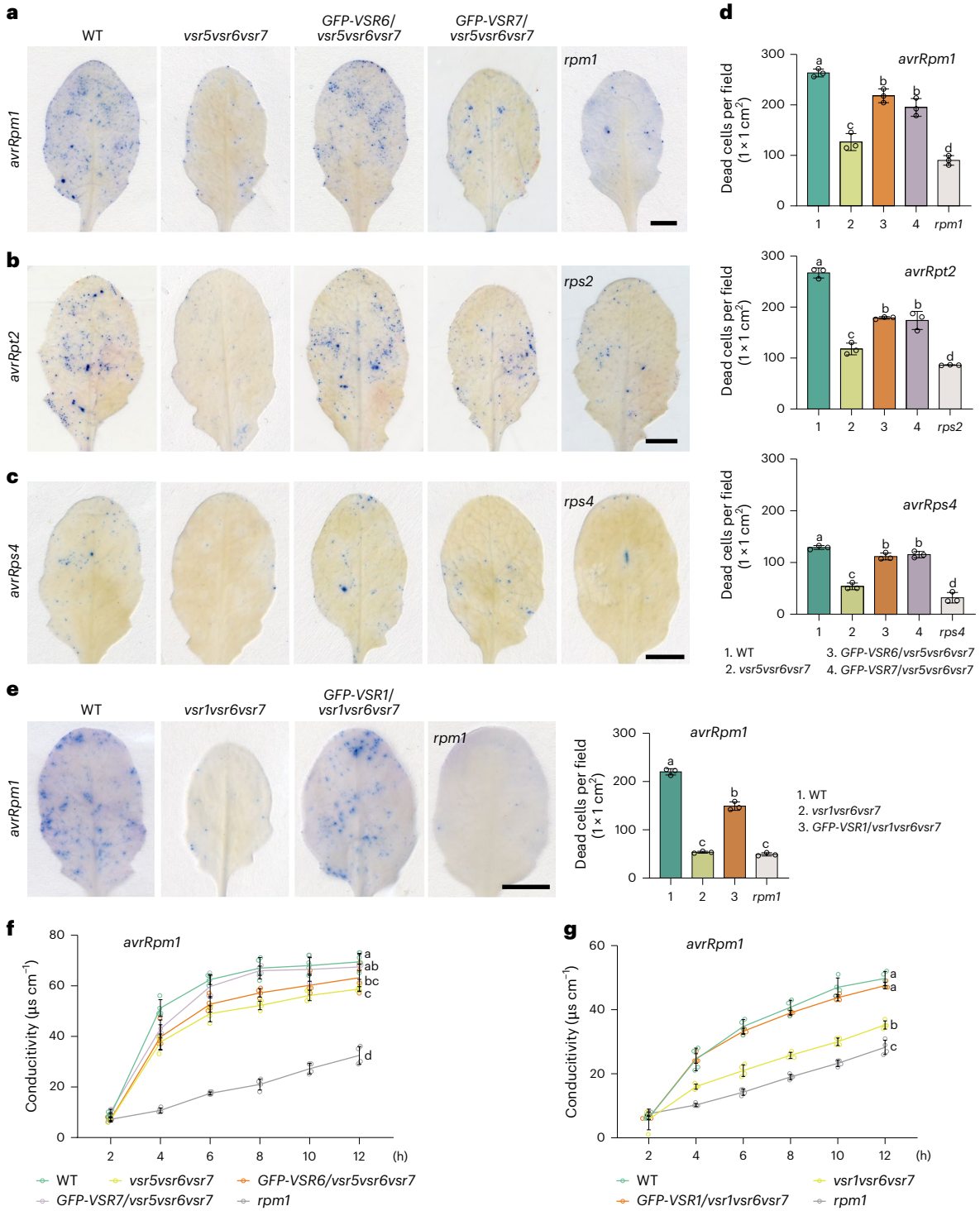

Fig. 3 | Bacteria-induced hypersensitive cell death is reduced in *vsr* mutants. **a**–**c**, Trypan blue staining of dead cells in the leaves of WT, *vsr5vsr6vsr7*, *GFP-VSR6/vsr5vsr6vsr7*, *GFP-VSR7/vsr5vsr6vsr7*, or the corresponding resistance gene mutants at 12 h after inoculation with *Pto* DC3000 *avrRpm1* (OD_{600} = 0.001) (**a**), at 24 h after inoculation with *Pto* DC3000 *avrRpt2* (OD_{600} = 0.002) (**b**) and at 12 h after inoculation with *Pto* DC3000 *avrRps4* (OD_{600} = 0.05) (**c**). Loss-of-function mutants of *RPM1* (*rpm1*), *RPS2* (*rps2*) or *RPS4* (*rps4*) served as additional controls. Note that the *vsr5vsr6vsr7* mutant had fewer dead cells than WT. Scale bars, 5 mm. **d**, Quantification of trypan blue staining intensity. Plants were stained with trypan blue and decolourized, and at least three randomly selected leaves were used for quantification. Results are presented as the number of necrotized cells compared with the total area of leaf blades analysed using ImageJ. Data are presented as means ± s.d. of three independent experiments. Different letters above bars indicate significant differences at $P < 0.05$, determined using one-way ANOVA with Fisher's LSD multiple comparisons test. **e**, Left: trypan blue staining of dead cells in the leaves of WT, *vsr1vsr6vsr7*, *GFP-VSR1/vsr1vsr6vsr7* and *rpm1* mutants at 12 h after inoculation with *Pto* DC3000 *avrRpm1* (OD_{600} = 0.001). Right: quantification of trypan blue staining intensity. Data are presented as means ± s.d. of three independent experiments. Different letters above bars indicate significant differences at $P < 0.05$, determined using one-way ANOVA with Fisher's LSD multiple comparisons test. Scale bar, 5 mm. **f**,**g**, Electrolyte leakage from dying and dead cells in the leaves of *vsr5vsr6vsr7* (**f**) or *vsr1vsr6vsr7* (**g**) plants and indicated complemented lines inoculated with *Pto* DC3000 *avrRpm1* (OD_{600} = 0.1). Data are presented as means ± s.d. of four biological replicates. Different letters indicate significant differences at 12 h after bacterial inoculation ($P < 0.05$, one-way ANOVA with Fisher's LSD multiple comparisons test). The experiments were repeated independently three times with similar results. Exact *P* values for statistical tests in **d**–**g** are provided as Source data.

https://doi.org/10.1038/s41477-025-02077-8

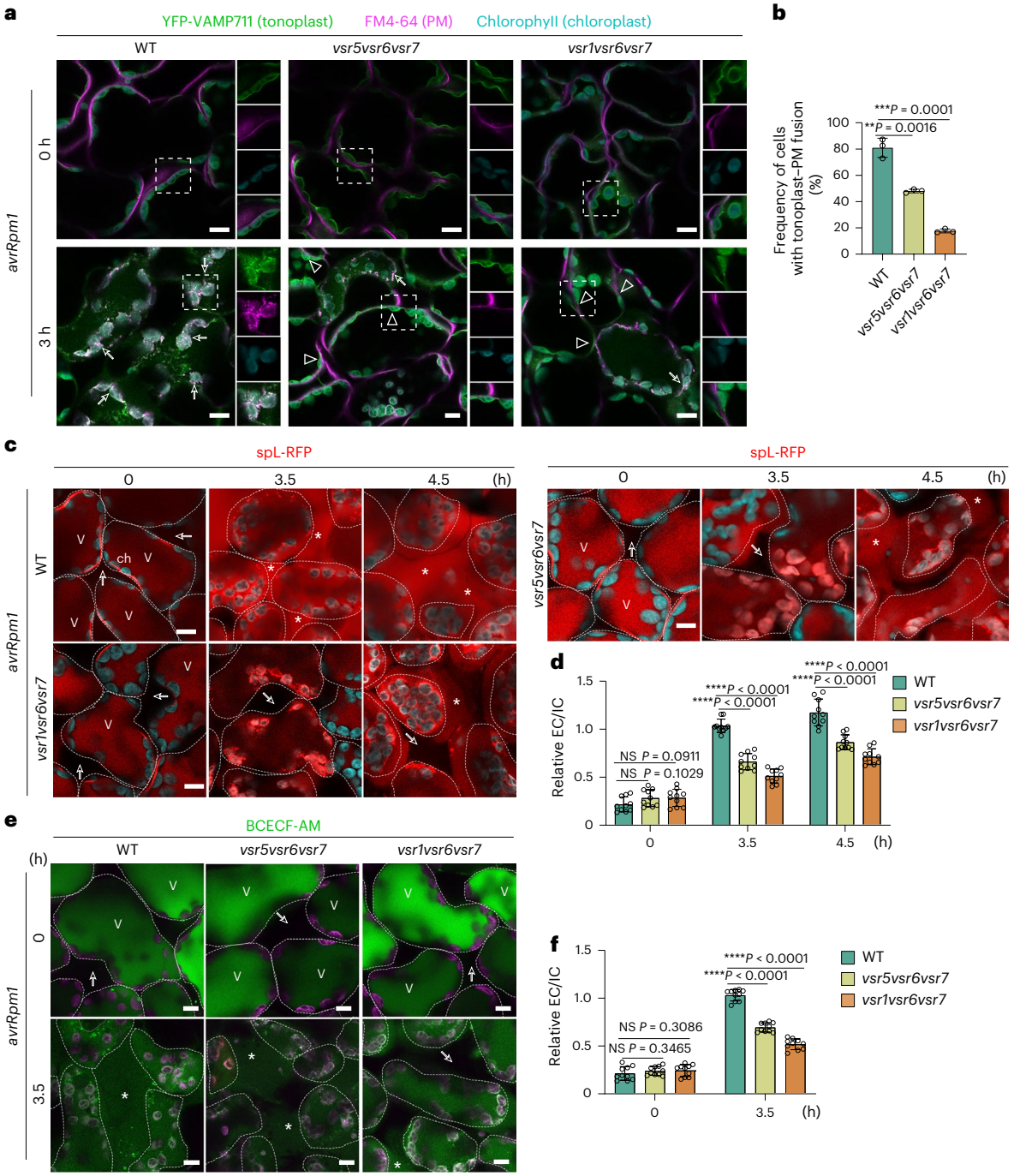

Fig. 4 | VSR deficiency suppresses fusion between tonoplast and PM after bacterial infection. a, Co-localization analysis of YFP-VAMP711 with FM4-64 staining in leaf mesophyll cells of WT, *vsr5vsr6vsr7* or *vsr1vsr6vsr7* immediately (0 h) or 3 h after inoculation of *Pto* DC3000 *avrRpm1*. Separated images of each channel in the white outlined area are shown on the right side (from top to bottom: GFP, RFP, chlorophyll and merged). Arrows indicate the co-localized fluorescence of YFP-VAMP711 and FM4-64, suggesting the fusion of vacuole with the plasma membrane. In most *vsr* mutant cells, FM4-64-stained PM remains separated from the YFP-VAMP711-labelled tonoplast structure (arrowheads). Scale bars, 10 µm. **b**, Frequency of cells with YFP-VAMP711 co-localized with FM4-64 signal in WT, *vsr5vsr6vsr7* and *vsr1vsr6vsr7* after 3 h inoculation of *Pto* DC3000 *avrRpm1*. The results were counted from 120 cells in three independent experiments. Data are presented as means ± s.d. $^{**}P < 0.01$, $^{****}P < 0.0001$, determined using two-tailed unpaired Student's *t*-test. **c**, Discharge of vacuolar marker protein spL-RFP to the extracellular space was impaired in *vsr5vsr6vsr7* and *vsr1vsr6vsr7* plants. Fluorescence images of mesophyll cells in leaves of indicated genotype expression with the spL-RFP at 0 h, 3.5 h and 4.5 h after inoculation with *Pto* DC3000 *avrRpm1*. Arrows and asterisks indicate the absence and presence of fluorescence signal in extracellular spaces, respectively. Dashed lines, cell boundaries; V, vacuole; ch, chloroplast with autofluorescence. Scale bars, 10 µm. **d**, Quantification of the relative EC to IC fluorescence intensity values of spL-RFP signal at the indicated times after inoculation with *Pto* DC3000 *avrRpm1*. NS, not significant. Data are presented as means ± s.d. of ten cells from three independent experiments. $^{****}P < 0.0001$; NS, $P > 0.05$, determined using one-way ANOVA with Fisher's LSD multiple comparisons test. **e**, BCECF-AM staining to assess vacuolar integrity. Fluorescence images of mesophyll cells in leaves of the indicated genotypes were captured at 0 h and 3.5 h after inoculation with *Pto* DC3000 *avrRpm1*. Arrows and asterisks indicate the absence and presence of fluorescence signal in extracellular spaces, respectively. Scale bars, 10 µm. **f**, Quantification of the relative EC to IC fluorescence intensity values of BCFCF-AM signal at the indicated times after inoculation with *Pto* DC3000 *avrRpm1*. Data are presented as means ± s.d. of ten cells from three independent experiments. $^{****}P < 0.0001$; NS, $P > 0.05$, determined using two-tailed unpaired Student's *t*-test (Source data).

In contrast, at 3.5 hpi, *vsr5vsr6vsr7* and *vsr1vsr6vsr7* plants exhibited decreased ($P < 0.001$) fluorescence diffusing into the ECS relative to WT plants (Fig. 4f). These results indicate that the dysfunction of these pathogen-inducible subgroup of *VSRs* leads to defects in the fusion between the tonoplast and the PM and in the subsequent release of vacuolar proteins into the ECS in response to infection.

The triple *vsr* mutants are impaired in autophagy processes

The integrity of vacuole morphology is closely related to hypersensitive cell death, which plays essential roles in bacterial ETI execution[24,59]. Therefore, we investigated whether the suppression of hypersensitive cell death in *VSR* mutants might be linked to alterations in the morphology and function of lytic endosomal compartments and the vacuole. Confocal observation of unchallenged *vsr5vsr6vsr7* or *vsr1vsr6vsr7* triple mutants did not reveal obvious changes in central vacuole morphology in cotyledon epidermal cells relative to WT plants (Extended Data Fig. 6a). In contrast, staining of lytic compartments in root cells with the acidophilic dye lysotracker red (LR) revealed frequent clusters of small vacuole-like compartments, which were separated from tonoplast labelled with YFP-VAMP711 punctae, in both *vsr5vsr6vsr7* and *vsr1vsr6vsr7* mutants but not in WT plants under standard growth conditions (Extended Data Fig. 6b). Moreover, the aberrant aggregation of LR-stained compartments in *vsr5vsr6vsr7* or *vsr1vsr6vsr7* triple mutants was further enhanced by the application of benzothiadiazole (BTH), a synthetic analogue of salicylic acid (Extended Data Fig. 6b). To determine whether the increase in aggregated LR-labelled compartments was due to changes in vacuolar pH, we measured it with the ratiometric pH indicator BCECF-AM[62]. The vacuolar pH in *vsr5vsr6vsr7* (pH 5.91 ± 0.06) and *vsr1vsr6vsr7* (pH 5.89 ± 0.06) root cells was similar to that of WT root cells (pH 5.93 ± 0.07), while it was increased in vacuoles of the *vha-a2 vha-a3* control plants (pH 6.37 ± 0.07) (Extended Data Fig. 6c). Thus, the obtained data suggest that VSRs are required for maintaining morphology of small lytic compartments but not pH in root cells.

Lysotracker dyes are employed to label autolysosome-like structures that are formed following the fusion of autophagosomes with endosomes or with vacuolar compartments for the degradation of autophagic cargo[59]. Given the contribution of autophagy to pathogen-triggered cell death[63], the abnormal morphology and potential dysfunction of late endocytic/lytic compartments observed prompted us to investigate whether autophagy is impaired in triple *vsr* mutants. An indicator of impaired autophagy is the increased gene expression of the autophagic markers[64]. Our transcriptomic studies identified 14 *ATGs* with transcript levels changing by >2-fold in *vsr5vsr6vsr7* and *vsr1vsr6vsr7* plants during the time course of infection with *Pto* DC3000 *avrRpm1*, relative to the WT plant before inoculation as a control (Fig. 5a). Furthermore, RT–qPCR confirmed increased expression levels of these *ATGs* in *vsr5vsr6vsr7* and *vsr1vsr6vsr7* lines compared with the WT during the time course of infection (Supplementary Fig. 3).

We next analysed the effect of VSR dysfunction on starvation-induced autophagy by incubating WT and mutant plants in the dark for prolonged periods, using the *atg5* mutant as an autophagy-defective control. In a detached leaf assay, *vsr5vsr6vsr7* and *vsr1vsr6vsr7* mutants, as well as *atg5* plants, showed hypersensitivity to dark treatment, exhibiting strongly increased chlorosis relative to WT plants after exposure to darkness for 7 days (Fig. 5b). Moreover, the increased senescence phenotype was partially complemented in the *GFP-VSR6/vsr5vsr6vsr7* and *GFP-VSR1/vsr1vsr6vsr7* lines, indicating that the loss of function of *VSRs* is responsible for the accelerated chlorosis (Fig. 5b). To investigate this phenomenon in whole plants, we incubated WT and *vsr5vsr6vsr7* or *vsr1vsr6vsr7* seedlings for 7 days in the dark. While WT seedlings were still green after 7 days of dark treatment, *vsr5vsr6vsr7* or *vsr1vsr6vsr7* seedlings became yellowish and had reduced chlorophyll content (Extended Data Fig. 7a,b). The dark-induced chlorosis in *vsr5vsr6vsr7* or *vsr1vsr6vsr7* could be partially complemented by *GFP-VSR7* or *GFP-VSR1*, respectively, indicating that the loss of corresponding *VSRs* is indeed the cause of these phenotypes. These results suggest that *vsr5vsr6vsr7* and *vsr1vsr6vsr7* mutants, similar to the previously reported *atg5* mutants, are defective in starvation-induced autophagy.

To determine the genetic interaction between *VSRs* and *ATGs* in plant immunity, we generated a *vsr5vsr6vsr7atg5* quadruple mutant and compared its immune responses with those of *vsr5vsr6vsr7* and *atg5*

Fig. 5 | VSRs are required for autophagy processes. a, Transcript levels ($\log_2$) of *ATGs* in WT, *vsr5vsr6vsr7* and *vsr1vsr6vsr7* plants after inoculation with *Pto* DC3000 *avrRpm1*. Heat map displays the relative expression level of *ATGs* of WT, *vsr5vsr6vsr7* and *vsr1vsr6vsr7* plants at different time points (1.5 h, 3 h and 6 h) as compared with WT (0 h) plants. **b**, Left: leaf detachment assay of indicated genotype plants. Detached leaves of 4-week-old plants were kept for 7 days on moist filter paper in darkness. The *atg5* mutant was used as a control. Right: quantification of chlorophyll contents in leaves of indicated genotypes. Data are presented as means ± s.d. of three independent experiments. Different letters above bars indicate significant differences at $P < 0.05$, determined by one-way ANOVA with Fisher's LSD multiple comparisons test. Scale bar, 1 cm. **c**, Disease symptoms on representative infected leaves were monitored 3 d after inoculation. Leaves of WT, *vsr5vsr6vsr7*, *atg5* and *vsr5vsr6vsr7atg5* after 3 days inoculation with *Pto* DC3000 expressing *avrRpm1* ($OD_{600} = 0.001$). The *vsr5vsr6vsr7atg5* leaves inoculated with indicated avirulent bacterial strain exhibit more severe chlorotic symptoms than other genotypes. A loss-of-function mutant of the corresponding resistance gene *RPM1* (*rpm1*) served as an additional control. Scale bars, 1 cm. **d**, Bacterial growth 3 d after inoculation with *Pto* DC3000 expressing *avrRpm1* ($OD_{600} = 0.001$) in the leaves of mutants shown in **c**. Each bar represents $\log_{10}$-transformed values of the mean ± s.d. of three biological replicates. Experiments were repeated three times with similar results. Different letters above bars indicate significant differences at $P < 0.05$, determined using one-way ANOVA with Fisher's LSD multiple comparisons test. **e**, Co-localization analysis of GFP-VSR1 with mCherry-ATG8e in leaf mesophyll cells of WT immediately (0 h) or 3 h after inoculation of *Pto* DC3000 *avrRpm1*. Separated images of each channel in the white outlined area are shown on the right side (from top to bottom: GFP, mCherry, chlorophyll and merged). Arrows indicate the co-localized fluorescence of GFP-VSR1 and mCherry-ATG8e. The percentage of mCherry-ATG8e with GFP-VSR1 co-localization is included at the bottom. Co-localization was quantified from ten individual leaves of three independent experiments. *n*, total numbers of analysed mCherry-ATG8e punctae. Scale bars, 10 μm. **f**, Immunoblot analysis of NBR1 accumulation upon infection with *Pto* DC3000 *avrRpm1*. Total proteins were extracted from 5-day-old *vsr5vsr6vsr7*, *vsr1vsr6vsr7*, WT and *atg5* seedlings at the indicated time points after infection with *Pto* DC3000 *avrRpm1* (0 h, 3 h and 6 h), followed by immunoblot analysis with anti-NBR1 antibody. The cytoplasmic marker anti-cFBPase, a ubiquitously expressed cytosolic fructose-1,6-bisphosphatase, is used as a loading control. The immunoblot intensity was normalized to the loading control of anti-cFBPase, and the first lane (WT, 0 h) was arbitrarily set to 1 (Source data). **g**, Accumulation and vacuolar delivery of autophagosome marker eYFP-ATG8e in WT, *vsr5vsr6vsr7* or *vsr1vsr6vsr7* plants after infection with *Pto* DC3000 *avrRpm1*. Confocal images are representative of leaf epidermal cells in 5-day-old seedlings before (−) and after (+) inoculation with *Pto* DC3000 *avrRpm1*, or with 0.5 μM Conc A (+Conc A) treatment for an additional 3 h, followed by confocal microscopy analysis. White arrows indicate eYFP-ATG8e punctae in the cytosol, and arrowheads indicate eYFP-ATG8e punctae inside the vacuole. Bottom right: quantification of the number of eYFP-ATG8e punctae in cytosol or vacuole. Data are presented as means ± s.d. of 30 individual cells from 3 independent experiments. Different letters above bars indicate significant differences at $P < 0.05$, determined using one-way ANOVA with Fisher's LSD multiple comparisons test. Scale bars, 20 μm. **h**, Immunoblot detection of the vacuolar delivery of eYFP-ATG8e after infection with *Pto* DC3000 *avrRpm1*. Total proteins were extracted from seedlings of indicated plants at the indicated time points (0 h, 3 h and 6 h) after inoculation, then subjected to immunoblot analysis with anti-GFP antibody to detect eYFP-ATG8e and the eYFP core. The cytoplasmic marker anti-cFBPase was used as a loading control. The ratio of the immunoblot intensity of free eYFP to eYFP-ATG8e was quantified in each sample. Immunoblot experiments (**f** and **h**) were repeated independently three times with similar results. Exact *P* values for statistical tests in **b**, **d** and **g** are provided as Source data.

https://doi.org/10.1038/s41477-025-02077-8

mutants. Inoculation with *Pto* DC3000 *avrRpm1* revealed enhanced susceptibility in all mutant lines compared with WT. Notably, the quadruple mutant showed severe disease symptoms, with greater chlorosis and tissue collapse than either *vsr5vsr6vsr7* or *atg5* single mutant (Fig. 5c). Quantitative analysis revealed a 2.56-fold increase ($P < 0.05$) in bacterial proliferation in *vsr5vsr6vsr7atg5* plants relative to *vsr5vsr6vsr7* mutants, but similar bacterial proliferation to that in *atg5* mutants (Fig. 5d). These results support the notion that defective

autophagy in the *vsr5vs6vsr7* mutant is what causes increased bacterial proliferation after infection with *Pto* DC3000 *avrRpm1*.

Having established the functions of VSRs during *P. syringae* infection, we next explored their subcellular dynamics during immune responses. Upon infection of *Pto* DC3000 *avrRpm1*, punctate structures of GFP-VSR1 underwent relocalization within 3 hpi, with a marked increase in co-localization with the autophagosome marker mCherry-ATG8e (from 0.5 ± 1.4% to 62.6 ± 3.8%) and a decrease in co-localization with the PVC/MVB marker mCherry-Rha1 (from 83.6 ± 2.8% to 60.1 ± 5.4%) (Fig. 5e and Extended Data Fig. 8a). In contrast, GFP-VSR1 remained largely dissociated from the Golgi or TGN markers both before and after infection (Extended Data Fig. 8b,c), demonstrating that GFP-VSR1 increased co-localization specifically with autophagosome markers. Intriguingly, the PVC/MVB marker mCherry-Rha1 exhibited partial association (28.8 ± 4.5%) with eYFP-ATG8e (Extended Data Fig. 8d) at 3 hpi, suggesting possible infection-stimulated rerouting or fusion of PVC/MVB to autophagosomes. Collectively, these findings highlight a relocalization of VSR1 from PVC/MVB to autophagosomes during immune response.

Further investigation into the impact of *VSR* deficiency on autophagic activity involved monitoring of the protein levels of the autophagic adaptor protein NBR1 whose vacuolar degradation serves as a marker for autophagic flux[65]. As expected, NBR1 levels remained low in untreated WT seedlings due to basal autophagy activity but were enhanced upon inoculation with *Pto* DC3000 *avrRpm1*. Importantly, *vsr5vsr6vsr7* and *vsr1vsr6vsr7* mutants showed constitutively increased NBR1 amounts (Fig. 5f and Extended Data Fig. 7c). In addition, NBR1 level in the *vsr5vsr6vsr7atg5* quadruple mutant was higher compared with those of *vsr5vsr6vsr7* and *atg5* mutants (Extended Data Fig. 7d). To distinguish whether early or late autophagic steps are affected in *vsr* mutants, we introduced eYFP-ATG8e into the triple *vsr* mutants for observation of autophagosome formation and detection of autophagic flux. We then infected a transgenic line expressing eYFP-ATG8e and found that *Pto* DC3000 *avrRpm1* stimulated the formation of YFP-labelled autophagosomal structures compared with the non-infected control (Fig. 5g). YFP-derived fluorescence before and 3 h after bacterial infection revealed accumulation of punctate autophagosome-like structures in leaves of *vsr5vsr6vsr7* and *vsr1vsr6vsr7* mutants, indicating that *VSR* deficiency does not impair autophagy initiation. However, we found enhanced accumulation of eYFP-ATG8e punctae in the cytosol of *vsr5vsr6vsr7* and *vsr1vsr6vsr7* mutants, compared with WT, suggesting that the mutations are blocking autophagy progression (Fig. 5g). Moreover, quantification of autophagosome numbers in vacuoles under concanamycin A (Conc A) treatment, which inhibits the degradation of autophagic cargo, further showed that the number of ATG8e punctae was decreased in the *vsr5vsr6vsr7* and *vsr1vsr6vsr7* mutants (Fig. 5g), indicating a disruption in autophagic flux.

Autophagic flux can be monitored by a GFP turnover assay, which analyses the cleavage efficiency of free eYFP from eYFP-ATG8e using immunoblotting with GFP antibodies[66]. We next monitored the eYFP-ATG8e fusion protein by immunoblotting after infection with *Pto* DC3000 *avrRpm1*. We observed that after infection with *Pto* DC3000 *avrRpm1*, the ratio of eYFP core to eYFP-ATG8e was upregulated in WT plants, but not in the *vsr5vsr6vsr7* and *vsr1vsr6vsr7* mutants (Fig. 5h and Extended Data Fig. 7e). Collectively, these findings suggest that *VSR* deficiency impairs the execution steps of autophagy-mediated vacuolar pathways.

VSRs participate in autophagic degradation of effector proteins

Effector proteins from various plant pathogens have been reported to target core autophagy machinery to manipulate this degradative pathway[27,67]. Conversely, effectors may be targeted by plant factors for autophagy-mediated degradation[29], but our current understanding of this process is very limited. To analyse the fate of effectors in plant cells, we transiently expressed GFP-tagged versions in seedlings and analysed their distribution after incubation for 24 h in darkness, which promotes the stabilization of fluorescently labelled protein in plant lytic compartments[68]. These effectors induced the ETI pathway in seedlings, as evidenced by trypan blue staining (Supplementary Fig. 4). In WT plants expressing avrRpm1-GFP, avrRpt2-GFP or avrRps4-GFP, a diffuse fluorescence pattern labelling the cell interior was observed (Fig. 6a), indicating that they are indeed delivered into the vacuole for degradation. Interestingly, the vacuole fluorescence of the effectors was decreased in the *vsr1vsr6vsr7* and *atg5* mutants (Fig. 6a, bottom right), indicating that their transport to the vacuole

Fig. 6 | VSRs contribute to autophagy degradation of effector proteins. **a**, Localization of avrRpm1-GFP, avrRpt2-GFP and avrRps4-GFP in WT, *vsr1vsr6vsr7* triple mutants and *atg5* mutant. Arabidopsis seedlings of the indicated genotypes were transiently transformed with GFP-fused effectors and visualized after 24 h dark treatment. Note the reduced fluorescence signal in lytic vacuoles (asterisks) in the *vsr1vsr6vsr7* and *atg5* mutant, compared with that in WT. Arrows indicate the PM localization of avrRpm1-GFP. Bottom right: quantification of the relative vacuole to cytosol fluorescence intensity values. Data are presented as means ± s.d. of ten cells from three independent experiments. $^{****}P < 0.001$, one-way ANOVA with Fisher's LSD multiple comparisons test. Scale bars, 10 μm. **b**, Immunoblot detection of the vacuolar delivery of GFP fusion of effectors in WT or *vsr1vsr6vsr7* triple mutants after dark treatment in **a**. Total proteins were extracted from seedlings of indicated plants, then subjected to immunoblot analysis with anti-GFP antibody to detect GFP fusion and the GFP core. Note the reduced GFP core (arrows) in the *vsr1vsr6vsr7* mutant, compared with that in WT (Source data). Arrowheads indicated the loading control. **c**, FRET efficiency analysis of the co-localized puncta between cerulean-ATG8e and the effectors (avrRpm1-YFP, avrRpt2-YFP or avrRps4-YFP). FRET efficiency was quantified using the AB approach. For each group, seven individual protoplasts were used for FRET efficiency quantification and statistical analysis. Data are presented as means ± s.d. of FRET efficiency. **d**, Co-IP analysis showing the interaction between ATG8e and avrRpm1, avrRpt2 or avrRps4. Arabidopsis protoplasts expressing YFP (lane 1), avrRpm1-YFP (lane 2), avrRpt2-YFP (lane 3), avrRps4-YFP (lane 4) or positive control SH3P2-YFP (lane 5) with 3×Myc-ATG8e were subjected to protein extraction and IP with GFP-trap, followed by immunoblotting with indicated antibodies. Arrowhead indicates ATG8e proteins co-IP by avrRpm1, avrRpt2 or avrRps4. **e**, Co-IP analysis showing the interaction between endogenous ATG8e and avrRpm1-GFP in WT or *rpm1* mutant plants. Arabidopsis seedlings expressing GFP (lane 1), *DEX::avrRpm1-GFP* in WT (lane 2), *DEX::avrRpm1-GFP* in *rpm1* (lane 3) or positive control SH3P2-GFP (lane 4) were subjected to DEX induction for 24 h, protein extraction and IP with GFP-trap, followed by immunoblot with indicated antibodies. Arrowhead indicates endogenous ATG8e proteins co-IP by avrRpm1-GFP in WT or *rpm1* mutant. **f**, NBR1 interaction with bacterial effectors avrRpm1, avrRpt2 and avrRps4 in *Nicotiana benthamiana* plants using a BiFC assay. NBR1 fused with an N terminus of YFP (YFPn) was co-expressed with avrRpm1, avrRpt2 or avrRps4 fused with C-terminus YFP (YFPc). Reconstituted YFP fluorescence, co-localized with autophagosome marker mCherry-ATG8e, indicates a positive interaction. The pair of SH3P2-YFPc and YFPn-NBR1 was used as control. The regions within the white outline are enlarged (right) (magnification: ×5). White arrows indicate punctae that co-localized with mCherry-ATG8e in the cytosol. Scale bars, 10 μm. **g**–**i**, *VSR* mutants impair the autophagy degradation of effectors. Confocal images of cotyledon cells from Arabidopsis seedlings of the indicated genotypes of mCherry-ATG8e transiently co-transformed with avrRpm1-GFP, avrRpt2-GFP or avrRps4-GFP. Note that in the *vsr5vsr6vsr7* and *vsr1vsr6vsr7* triple mutants, accumulated mCherry-ATG8e co-localized puncta (arrows) in cytosols, compared with diffuse cytosolic signal in WT. Scale bars, 10 μm. **j**, Quantification of the number of puncta of avrRpm1-GFP, avrRpt2-GFP or avrRps4-GFP per cell in plants of indicated genotype. Data are presented as means ± s.d. of puncta number obtained from 20 individual cells of 3 independent experiments. $^{****}P < 0.001$, one-way ANOVA with Fisher's LSD multiple comparisons test. The experiments in **b**–**f** were repeated independently three times with similar results.

https://doi.org/10.1038/s41477-025-02077-8

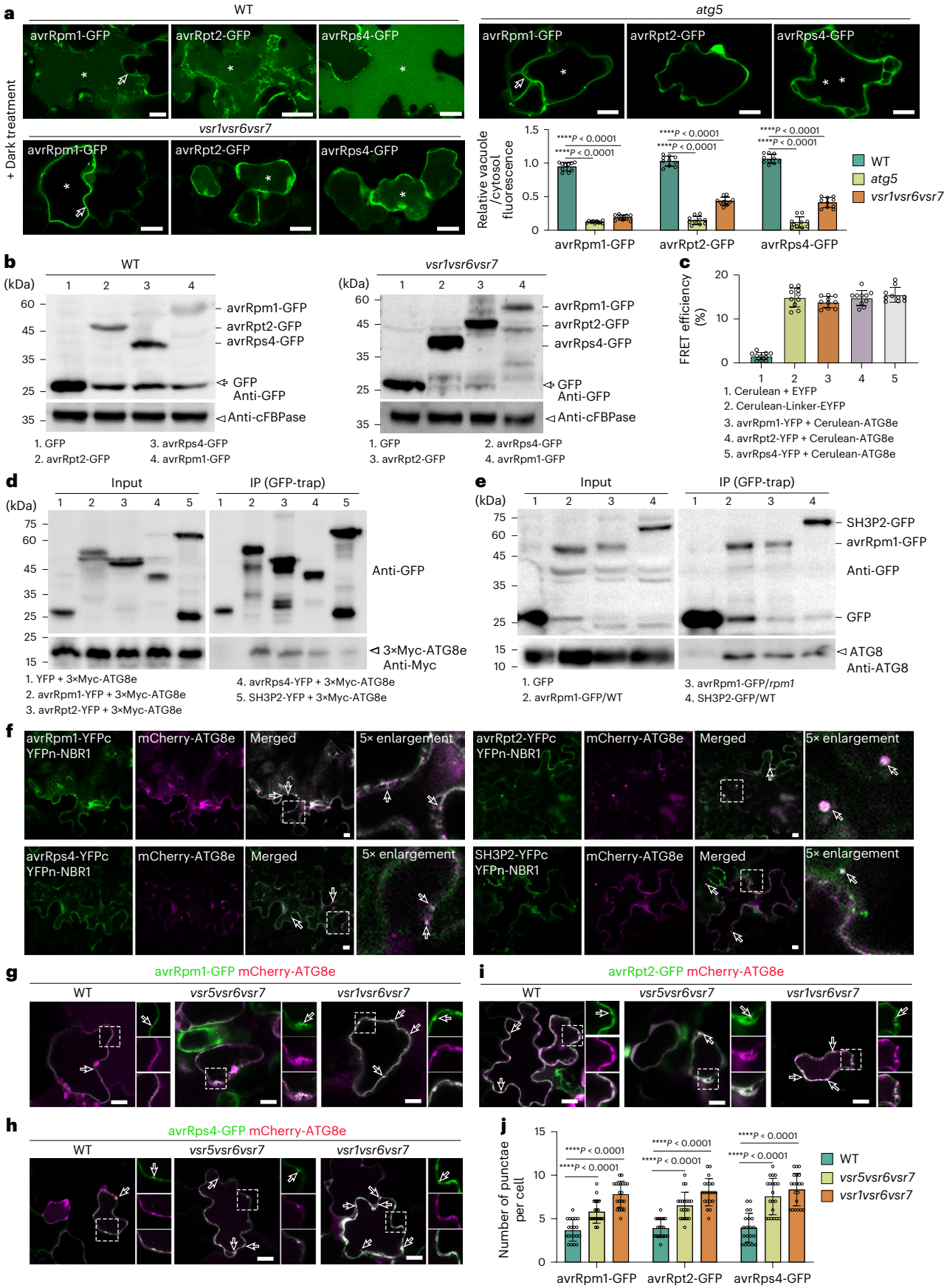

requires VSRs and that it occurs through autophagy. To assess effector degradation, we extracted total proteins from seedlings transiently expressing GFP-tagged effectors and performed immunoblot analysis using anti-GFP antibodies. In WT seedlings, we observed the accumulation of a free GFP-core fragment at 24 hpi (Fig. 6b), indicating that the GFP-tagged effectors are degraded in the vacuole. However, this GFP-core accumulation was reduced in the *vsr1vsr6vsr7* triple mutant compared with WT (Fig. 6b). Taken together, the obtained data indicate that the effectors are delivered into the vacuole in a VSR-dependent manner for their autophagy-mediated degradation.

To further support the idea that the effectors are the targets for autophagy, we tested for co-localization of avrRpm1-YFP, avrRpt2-YFP and avrRps4-YFP effectors with the autophagosome marker cerulean-ATG8e in transiently transformed Arabidopsis protoplasts. We observed the avrRpm1-YFP signal at the PM and in intracellular punctae labelled with cerulean-ATG8e (Extended Data Fig. 9a). Likewise, avrRpt2-YFP and avrRps4-YFP showed a diffused pattern in the cytosol and partially co-localized with cerulean-ATG8e on the autophagosome membrane (Extended Data Fig. 9b,c). However, the punctae of YFP signals were largely separated from the PVC/MVB marker RFP-Rha1 (Extended Data Fig. 9d). FRET–AB analysis revealed that avrRpm1-YFP, avrRpt2-YFP and avrRps4-YFP, but not the control EYFP, showed strong interactions with cerulean-ATG8e in the punctate compartments (Fig. 6c). In addition, 3×Myc-ATG8e co-immunoprecipitated with avrRpm1-YFP, avrRpt2-YFP or avrRps4-YFP, but not with the YFP negative control (Fig. 6d). Indeed, the fusion protein avrRpm1-GFP co-immunoprecipitated with endogenous ATG8 proteins when expressed in either WT or *rpm1* mutant plants (Fig. 6e). Thus, these findings further support the association of bacterial effectors with the autophagic machinery and suggest that their interaction does not require ETI activation. In the autophagy process, NBR1 acts as a selective cargo receptor for degradation of ubiquitinated substrates. To validate the effectors as substrates for autophagic degradation in planta, we tested for their interaction with NBR1 using bimolecular fluorescence complementation (BiFC) assays. Reconstitution of the YFP signal suggested that avrRpm1, avrRpt2 and avrRps4 effectors interact with NBR1 in planta at mCherry-ATG8e-labelled autophagosomes (Fig. 6f and Extended Data Fig. 9e). Moreover, the avrRpm1, avrRpt2 and avrRps4 effectors also interacted with ATG8e in BiFC assays (Extended Data Fig. 9f).

After having established that the avrRpm1, avrRpt2 and avrRps4 effectors are most likely targets for NBR1- and ATG8e-dependent autophagy, we tested whether mutations in *VSRs* alter their distribution in autophagosomes. In WT cells, avrRpm1-GFP, avrRpt2-GFP and avrRps4-GFP localized in mCherry-ATG8e-decorated autophagosomes (Fig. 6g–i). Likewise, avrRpm1-GFP also localized in mCherry-ATG8e-decorated autophagosomes in *vsr1vsr6 vsr7* and *vsr5vsr6vsr7*, but the number of punctae per cell was substantially ($P < 0.0001$) increased in the triple mutants relative to WT plants, particularly in *vsr1vsr6vsr7* (Fig. 6j). Similarly, an increased number of punctae with co-localized mCherry-ATG8e and avrRpt2-GFP or avrRps4-GFP was observed in *vsr5vsr6vsr7* or *vsr1vsr6 vsr7* relative to WT plants (Fig. 6j). These results are consistent with the reduced levels of the effectors found in vacuoles of the *vsr* mutants (Fig. 6a). To further confirm the autophagic degradation of effectors, we generated dexamethasone (DEX)-inducible lines of avrRpm1-GFP, avrRpt2-GFP and avrRps4-YFP and examined their co-localization with the autophagosome marker mCherry-ATG8e. After DEX induction, punctate structures of the effectors were observed in the cytosol and co-localized with mCherry-ATG8e in WT plants (Extended Data Fig. 10a). In addition, in the presence of Conc A, mCherry-ATG8e-positive puncta and GFP fusion of effectors accumulated in the vacuole lumen. To test whether dysfunction of the *VSRs* perturbs the vacuolar transport of effectors, we generated the *DEX::avrRps4-YFP* in the *vsr1vsr6vsr7* mutant. Interestingly, the vacuolar targeting of avrRps4-YFP was significantly impaired in *vsr1vsr6vsr7*, with a reduced number of puncta ($P < 0.0001$) in the vacuole lumen after Conc A treatment compared with WT (Extended Data Fig. 10b,c). Taken together, these results reveal the role of NBR1, ATG8e and VSRs in autophagosome-mediated degradation of bacterial effectors in the vacuole.

Discussion

Vacuolar sorting receptors play a crucial role in sorting seed storage proteins or lytic enzymes to vacuoles within the secretory pathway, by directly interacting with the cargo through their NT luminal domain and with adaptor protein (AP) complexes AP-1 or AP-4 (which facilitate anterograde transport of the receptor–cargo complex) through their cytosolic CT domain[69–71]. The dynamic trafficking of VSRs ensures the precise sorting of proteins in the secretory pathway and the maintenance of cellular homeostasis, which are essential in various developmental processes and osmotic stress responses[15,31,32,72]. In addition, it was previously reported that *VSR6* and *VSR7* are among a few direct targets for transcriptional activation by NPR1 (ref. 33), but whether and how VSRs contribute to plant immunity had remained unknown.

Here we identified the involvement of VSRs in plant pathogen defence by demonstrating the following: (1) A subgroup of Arabidopsis *VSRs* is transcriptionally induced during infection with *P. syringae*, which results in higher VSR protein levels; (2) VSRs bind cell death-related hydrolytic enzymes and dysfunction of the pathogen-responsive *VSRs*, specifically in the *vsr5vsr6vsr7* and *vsr1vsr6vsr7* mutants, leading to defects in the transport of these enzymes and resulting in their secretion into the ECS; (3) Deficiency in pathogen-responsive *VSRs* interferes with tonoplast–PM fusion and hypersensitive cell death activated upon infection with avirulent *P. syringae* strains, resulting in increased plant susceptibility characterized by stronger disease symptoms and higher bacterial loads; (4) Depletion of *VSRs* leads to autophagy defects, resulting in accumulation of bacterial effector proteins in autophagosomes and their reduced turnover in the vacuole. These observations would seem to argue that the subgroup of pathogen-inducible *VSRs* plays multiple roles in ETI, mediating vacuolar sorting of immunity-related vacuolar lytic enzymes, vacuole to PM fusion and hypersensitive cell death, as well as degradation of effector proteins through the autophagy pathway.

The ETI in response to *P. syringae* pv. tomato (*Pto*) DC3000 harbouring *avrRpm1* or *avrRpt2* is conditioned by the CC-NB-LRR-type resistance (*R*) protein RPM1 or RPS2, respectively, whereas ETI response elicited by *Pto* DC3000 *AvrRps4* requires the TIR-NB-LRR class *R* protein RPS4 (refs. 58,73,74). A common theme in the hypersensitive response (HR) triggered by these CC-NB-LRR and TIR-NB-LRR R-genes is the requirement of vacuole-mediated execution steps[22]. RPS2-dependent HR involves fusion of the tonoplast with the PM and discharge of vacuolar hydrolytic enzymes into the ECS[24]. RPS4-dependent HR engages autophagy mechanisms[63], which require collapse of vacuolar membranes and the release of hydrolytic enzymes into the cytosol[75]. Interestingly, both forms of vacuolar cell death seem to be induced upon RPM1 activation[24,63]. The results presented here strongly suggest that VSR deficiency interferes both with vacuolar processes and with autophagic flux during the HR, affecting the execution steps of autophagy- and vacuole fusion-mediated cell death. This may explain the severe suppression of the HR mediated by either TIR-NB-LRR or CC-NB-LRR proteins in *vsr* mutants. The contribution of VSRs to plant immunity presented here is also distinct from that reported for the VSR-interacting regulators AP-2 and AP-4, which participate in ETI triggered by RPM1 and RPS2 but not by RPS4, possibly by regulating clathrin-mediated endocytosis of PM-localized RPM1 and RPS2 (refs. 76,77). However, our data are consistent with previous research suggesting that the retromer component VPS35 homologues, which are responsible for VSR recycling, contribute to certain forms of NB-LRR protein-mediated autoimmunity and pathogen-triggered HR. Retromer deficiency is known to cause defects in late endocytic/lytic compartments and impairs vacuolar

processes associated with autophagy[59]. In mammalian and yeast cells, the retromer complex is a regulator of the rerouting of ATG9-containing vesicular carriers toward sites of autophagosome formation[78,79]. Given the interaction between VSRs and the retromer complex in Arabidopsis, it would be valuable in the future to investigate the localization of the retromer in *vsr* mutants, and conversely, to identify the presence of VSRs in retromer mutants during the autophagic process.

VSRs are involved in autophagy-mediated cell death during ETI

Autophagy, a conserved intracellular trafficking and degradation process, has been implicated in basal immunity as well as in some forms of immune receptor-mediated vacuolar cell death[63,67]. Our finding that deficiency of VSRs in *vsr5vsr6vsr7* and *vsr1vsr6vsr7* mutants exhibits additional defects in starvation-induced autophagy (Fig. 5 and Extended Data Fig. 7) further implicates important functions of VSR components and trafficking in autophagic mechanisms. In this regard, a recent study demonstrated that VPS10, a vacuolar cargo sorting receptor in yeast, plays a novel context-dependent role in autophagy, particularly in the trafficking and maturation of the aspartyl-protease Pep4 and its impact on the proteolytic activity of the vacuole[80]. In our screen for VSR cargoes upregulated after bacterial infection, we found a Pep4 homologue in Arabidopsis that localizes to the PVC/MVBs and vacuole (Extended Data Fig. 2d). This finding suggests that a common Pep4-mediated mechanism for context-dependent autophagy regulated by vacuolar sorting receptors may be conserved from yeast to plants.

In plants, effector proteins from various plant pathogens have been found to perturb or hijack the autophagy pathway to attenuate plant immune reactions[29,67]. More specifically, plant pathogenic bacteria have been shown to utilize effectors to modulate autophagic degradation[81,82]. Our findings demonstrate that the avrRpm1, avrRps2 and avrRps4 effectors interact with the autophagic adaptor proteins NBR1 and ATG, and are targeted into vacuole for degradation. The flux of effectors into the vacuole is hampered in *vsr5vsr6vsr7* and *vsr1vsr6vsr7* mutants, supporting a role of VSRs in their autophagic degradation. Considering the evidence that avrRpm1, avrRps2 and avrRps4 interact with the selective cargo receptor NBR1, it is likely that their autophagy is triggered by ubiquitination, as has been suggested for XopL, another bacterial effector that also interacts with NBR1 (ref. 27). Hence, it would be interesting to analyse the ubiquitin status of avrRpm1, avrRps2 and avrRps4 during infection in WT and *vsr* mutant plants. In addition, it will be important to investigate whether VSRs may play a role beyond autophagy in turnover of bacterial effectors, especially in the trafficking of downstream components of ETI or PTI, which eventually function synergistically to provide resistance against pathogens[83]. Indeed, endocytic trafficking also plays a major role in plant immunity[4]. Moreover, this additional function would be consistent with the fact that *vsr* mutants can partially perturb PTI responses (Extended Data Fig. 4), which would not be due to a function in autophagy, since autophagy deficiency does not affect PTI responses[84]. Thus, further studies should be conducted to investigate whether the effectors are degraded by other additional mechanisms such as endocytosis or proteasome-mediated degradation.

Vacuolar hydrolytic enzymes for hypersensitive cell death and immunity

Understanding the intricate roles of vacuolar enzymes is essential for unravelling the molecular mechanisms underlying plant immunity and hypersensitive cell death. One of the key groups of enzymes we identified in this screening is the PLCPs. Recent research has emphasized the pivotal role of PLCPs in plant immunity, as they are crucial for providing full resistance to various pathogens[48]. When activated, PLCPs trigger a wide range of defence responses, including plant cell death. Although plants contain numerous PLCPs localized in different compartments, including vacuole, ER or apoplast, the mechanisms by which specificity is achieved remain largely elusive. According to our subcellular localization analysis and protein–protein interaction assays, the 11 pathogen-inducible PLCPs identified here are sorted by VSR proteins and primarily localized in the vacuole.

In addition to PLCPs, peroxidases (PRX33, PRX34 and PRX37) and endochitinases (PR3 and PR4) are highly induced in host plant tissues during pathogen infection (Extended Data Fig. 2a), which is consistent with previous microarray data indicating the upregulation of class III PRXs and chitinases under pathogen infection[85]. Class III peroxidases have been classified as secretory PRXs due to the presence of an N-terminal polypeptide that directs them to the extracellular space, and the presence of a C-terminal polypeptide has been shown to target class III PRXs to the vacuole[25]. PR3, PR4, PRX33 and PRX34 have been found in previously published vacuolar protein databases[25]. Indeed, our in vivo confocal observation has revealed that PRX33, PRX34 and PRX37 as well as endochitinase (PR3 and PR4) are localized in the vacuole (Extended Data Fig. 2d). Thus, peroxidases and endochitinase may be stored in the vacuole and released upon pathogen attack to degrade the cell walls of invading pathogens or reinforce the plant cell wall by catalysing the formation of lignin and suberin[86], thereby restricting pathogen growth and spread within the plant. Our results support that GRX (also known as GRXC4) is a soluble protein containing an N-terminal cleavable signal peptide[87] that targets it to the endomembrane system. Our confocal microscopy analysis shows that GRX-GFP exhibits a punctate localization pattern co-localizing with the PVC/MVB marker mRFP-VSR2, along with diffuse signals in the vacuole (Extended Data Fig. 2d). Consistent with this, our previous study has demonstrated that GRX is a VSR-mediated cargo protein, possessing a hydrophobic VKKTI sequence that functions as a vacuolar sorting determinant[14]. Given the established role of vacuolar proteins in plant–pathogen interactions, future studies should investigate how this vacuole-localized GRX contributes to immune responses against pathogens.

On the basis of the findings of this study and previous literature in plants, we propose the following working model of VSR function in plant immunity (Supplementary Fig. 5): (1) VSRs are type-I integral membrane proteins that play a crucial role in the secretory pathway of plant cells. These receptors are responsible for selectively sorting cargo proteins, particularly hydrolytic enzymes, into lytic vacuoles for degradation, which thus contribute to maintaining cellular homeostasis and regulating protein turnover; (2) After infection with *P. syringae*, cells perceive secreted type-III effectors and launch an ETI response that includes the induced expression of VSR proteins, to sort cell death-related proteinase into the vacuole and trigger hypersensitive cell death through membrane fusion between the tonoplast and PM; (3) The selective autophagic receptor NBR1 and ATG8 proteins interact with bacterial effector proteins, promoting their VSR-dependent autophagic degradation in the vacuole.

It is established that the PVC/MVB fuses with autophagosomes to form amphisomes, which are hybrid organelles critical for autophagic cargo delivery[88,89]. In this study, our data showed that the PVC/MVB marker protein Rha1 partially co-localizes with ATG8-labelled autophagosomes after *P. syringae* infection (Extended Data Fig. 8d). In addition, we also observed that VSRs are relocalized from PVC/MVB to ATG8-positive autophagosomes after infection (Fig. 5e). Future studies should aim to determine whether the VSR-ATG8 co-localization results from the recruitment of VSRs to autophagosomes or via their incorporation into newly formed amphisomes. Furthermore, it is crucial to further identify other VSR-interacting proteins that are required to regulate lytic enzyme and effector trafficking in the ETI process. In addition, it will be interesting to identify factors or signalling molecules that may regulate the distribution of VSRs between endosomes in the secretory pathway in sorting hydrolytic enzymes for hypersensitive cell death or into autophagosomes for effector elimination.

Methods

Plasmid construction

Double restriction enzyme digestion (Takara) or recombination (Vazyme) methods were performed to clone corresponding genes to plasmids. To generate constructs for transient expression in Arabidopsis protoplast, corresponding genes were amplified and cloned into pBI221 vectors modified to contain YFP, cerulean, mRFP, 3×Myc, and tags under 35S or UBQ10 promoter[90]. For making *VSR1pro::GFP-gVSR1*, *VSR5pro::GFP-gVSR5*, *VSR6pro::GFP-gVSR6* and *VSR7pro::GFP-gVSR7* transgenic plants, the native promoter and genomic DNA of indicated genes were fused with fluorescent proteins and cloned into pCAMBIA1300 using the recombination method. For the subcellular localization analysis of identified cargo proteins in cotyledon cells of Arabidopsis seedlings, the coding sequence of respective genes were PCR amplified and cloned into the pre-made pCAMBIA1300 backbone with mRFP fusion. For expression of tonoplast marker, constructs of VAMP711 were made by PCR cloning into the binary vector pCAMBIA1300 with YFP fusion. For expression of effector proteins, constructs of avrRpm1, avrRpt2 or avrRps4 were made by PCR cloning of the respective effector gene into the vector pBI221 and pCAMBIA1300 with GFP fusion. The coding region was further cloned into pTA7002-DEX vector for plant transformation. For BiFC constructs, the effectors, ATG8e, NBRI and SH3P2 were PCR amplified and cloned into the pre-made YFPn or YFPc vectors[91]. RD21A-YFP and RDL1-YFP were constructed previously[2]. All constructs were verified by Sanger sequencing. Primers used for plasmid construction, genotyping, or RT–qPCR are listed in Supplementary Table 2.

Plant materials

The Arabidopsis ecotype Col-0 T-DNA insertional mutants *vsr1-2* (GABI_503A05), *vsr2* (SALK_082962), *vsr4* (SALK_094467), *vsr5* (SALK_044991), *vsr6* (SAIL_338_H03) and *vsr7-3* (SAIL_1158_H09) were generated as previously described[31]. Arabidopsis *atg5* (SAIL_129_B07)[66], *vha-a2 vha-a3* (ref. 92), *rpm1-3* (ref. 93), *rps2-101C*[94] and *rps4* (ref. 95) were described previously. Double or triple mutants were generated by crossing and screened by genotyping PCR. The *vsr2VSR3*^{Cas9} *VSR4*^{Cas9}*-1* knockout line was produced by editing *VSR3* and *VSR4* in the *vsr2* T-DNA insertion mutant background, using an egg cell-targeting CRISPR-Cas9 system[60]. To generate the transgenic plants, all plasmids were introduced into *Agrobacterium tumefaciens* strain GV3101 and transformed into WT or mutants by floral dip. Arabidopsis WAVE lines stably expressing fluorescent protein-tagged organelle markers for protein subcellular localization were obtained from NASC. Fluorescent tagged transgenic plants in WT or indicated mutants were generated using transgenes or by crossing.

Plant growth and chemical treatments

Surface-sterilized Arabidopsis seeds were grown on plates with half-strength Murashige and Skoog (MS) medium (pH 5.7) with 1% (w/v) sucrose and 0.8% (w/v) agar at 22 °C under a long-day (16 h light/8 h dark) or short-day (8 h light/16 h dark) photoperiod. For phenotype analysis, 6-day-old seedlings on plates or 24-day-old plants on soil were observed and quantified. FM4-64 dye staining and uptake experiments and image collection were performed as previously described[90]. BTH (100 μM) was added to the liquid medium with seedlings for 6 h before confocal laser scanning microscopy (CLSM) observation. The seedlings were stained with 2 μM lysotracker red for 15 min before CLSM imaging. BCECF-AM (10 μM) was added to the liquid medium with leaves for 1 h before CLSM observation. For DEX induction in liquid medium, seedlings were transferred to liquid MS with ethanol as control or 10 μM DEX for indicated time before CLSM observation or protein extraction.

Bacterial strains and pathology tests

Pseudomonas syringae pv. tomato virulent strain DC3000 carrying the empty vector pVSP61 (*Pto* DC3000 EV), along with congenic avirulent strains (*Pto* DC3000 expressing *avrRpm1*, *avrRpt2* or *avrRps4*) and *Pto* DC3000 *hrcC*$^{-}$ were used in this study. The bacteria were cultured in King's B medium, washed twice in 10 mM $MgCl_2$, and then resuspended at optical density at 600 nm (OD_{600}) = 0.001 or 0.005 for plant inoculation in growth assays and trypan blue staining. For the electrolyte leakage assay, the bacteria were resuspended at OD_{600} = 0.1, and for confocal microscopy analysis, the suspension was at OD_{600} = 0.05. Inoculation of bacterial suspension was performed on the abaxial sides of 4–5-week-old Arabidopsis leaves using needleless syringes. Bacterial growth was monitored as previously described[24].

Trypan blue staining

Trypan blue staining was conducted as described with modification[77]. Briefly, inoculated leaves were imbibed with staining solution (1 ml lactic acid, 1 ml glycerol, 1 ml water-saturated phenol, 1 ml water and 1 mg trypan blue) for no more than 1 h at room temperature. The samples were then decolourized in 100% ethanol for at least 1 day.

Electrolyte leakage assay

The electrolyte leakage assay was conducted as described[24]. Four discs, each with a diameter of 7.5 mm, were excised from the leaves after bacterial inoculation. These discs were then floated in 2 ml of distilled water for 30 min, transferred to fresh distilled water and incubated at 22 °C. Water conductance was measured using an electrical conductivity metre (EC-33, Horiba).

Callose deposition

Callose staining was performed essentially as described[77]. Leaves were fixed and destained in 1:3 acetic acid:ethanol until the material was transparent. Fixed and destained leaves were washed in 150 mM K_2HPO_4 for 30 min. Then leaves were incubated for at least 2 h in 150 mM K_2HPO_4 and 0.01% aniline blue, and observed using ultraviolet illumination at 370–410-nm excitation and 450–500-nm emission wavelengths under a Zeiss LSM880 confocal microscope. Greyscale images of callose-stained leaves were used to quantify signal intensities using ImageJ software.

Transient expression in Arabidopsis

The Arabidopsis suspension cell line, plant system biology dark type culture (PSB-D), was maintained through subculture every 5 days. Detailed procedures for isolating protoplasts and conducting transient expression were described previously[96]. The protoplasts transferred with indicated plasmids were then incubated at 23 °C for 12 h before confocal imaging analysis or protein extraction.

Agrobacterium-mediated transient gene expression in Arabidopsis seedlings was described previously[17]. Briefly, *Agrobacterium* strain PMP90 carrying the designated binary vector was cultured at 28 °C and 200 r.p.m. for 20 h, followed by adjustment of the concentration to OD_{600} = 1.5 in 1/2 MS liquid medium. Four-day-old seedlings with the specified genotype were submerged in the *Agrobacterium* culture and subjected to vacuum infiltration twice for 1 min each. Subsequently, the *Agrobacterium* solution was removed, and the seedlings were transferred to half-strength MS medium for an additional 2 days of incubation before confocal microscopy imaging.

Confocal microscopy and FRET analysis

Five-day-old Arabidopsis seedlings or 5-week plant leaves with indicated genotypes were collected and visualized using a Leica TCS SP8 or Zeiss 880 confocal laser scanning microscope. Imaging was performed with a ×63 (NA 1.20) water immersion objective using sequential acquisition. For each experiment, 10 individual samples were observed and confocal imaging represented >75% of the samples to reveal similar expression levels and patterns. Images were processed using Adobe Photoshop software. Total punctae numbers of eYFP-ATG8e were

manually counted[17]. Co-localization and punctae number were quantified from at least five individual samples.

FRET–AB analysis was conducted on the Leica SP8 confocal system[97]. The protoplasts isolated from PSB-D cells, transiently expressing cerulean and YFP fusion proteins, were used for photobleaching at 514 nm laser with a speed of 200 Hz at full power intensity. The fluorescence intensity of the cerulean donor was captured and recorded before and after bleaching a region of interest containing YFP fusions until the intensity dropped below 10% of the initial level. FRET efficiency was calculated using the formula $Ef = 100 \times (D_{post} - D_{pre})/D_{post}$, where D_{pre} and D_{post} represent the fluorescence intensity of cerulean and its fusions before and after bleaching, respectively. FRET efficiency quantification and statistical analysis were conducted on a minimum of 10 protoplasts. Cerulean–EYFP fusions were used as positive control, and co-expressed free cerulean and EYFP served as the negative control.

pH measurements

The vacuolar pH of 5-day-old seedlings was assessed by utilizing the fluorescent cell-permeant dye BCECF-AM at 10 µM. Following a 1-h staining period at 22 °C in darkness, the seedlings were washed for 10 min in media. BCECF fluorescence was visualized using a Zeiss 880 confocal laser-scanning microscope, with excitation at 405 and 488 nm, and emission detection between 530 and 550 nm. Ratio images were created using the ion concentration tool in the Zeiss LSM Confocal software, and image processing was carried out using Adobe Photoshop software. The ratio values were determined using ImageJ. The integrated pixel density was quantified, with values from the 488-nm-excited images divided by those from the 405-nm-excited images. This ratio was then utilized to calculate the pH on the basis of a calibration curve according to previously described procedures[92].

Chlorophyll content measurement

Chlorophyll was extracted from both seedlings and leaves using 80% acetone (v/v). The content was determined spectrophotometrically at wavelengths of 663 nm and 645 nm, followed by calculation.

BiFC

For BiFC experiments, cultures of *Agrobacterium* strain GV3101 carrying BiFC constructs and control constructs were grown overnight at 28 °C in Luria-Bertani medium[91]. The harvested bacteria were resuspended in infiltration buffer (10 mM MES, 10 mM $MgCl_2$ and 150 µM acetosyringone) and allowed to incubate at room temperature for 2 h. Bacterial suspensions with $OD_{600} = 1$ were mixed in various combinations at equal ratios and infiltrated into the abaxial sides of 4-week-old leaves of *Nicotiana benthamiana*. Confocal microscopy imaging of the infiltrated leaves was performed at 36 to 40 h post infiltration.

Protein preparation

To extract protein from protoplasts, protoplasts transformed with indicated plasmids were first washed with 250 mM NaCl, followed by centrifugation at 100 *g* for 10 min to collect cells. Cells were resuspended in ice-cold lysis buffer containing 25 mM HEPES, 150 mM NaCl, 1 mM $MgCl_2$, 1,000 µM $CaCl_2$, 0.5% (v/v) Triton X-100 and 1× Complete Protease Inhibitor Cocktail (Roche) (pH 7.1). The total cell extracts were then centrifuged at 16,000 *g* for 10 min at 4 °C, followed by addition of SDS loading buffer.

For the protein extracted from seedlings, 5-day-old or 12-day-old Arabidopsis seedlings were ground in liquid nitrogen, added with lysis buffer containing 0.5% (w/v) Triton X-100 and then centrifuged at 16,000 *g* for 10 min at 4 °C. The supernatant was then extracted, boiled in sample loading buffer at 55 °C or 100 °C for 10 min and subjected to immunoblotting on 12% (w/v) SDS–PAGE gels.

Immunoprecipitation and immunoblotting

Transformed protoplasts were initially diluted with 3-fold volumes of 250 mM NaCl and then collected by centrifugation at 100 *g* for 10 min. Subsequently, the protoplasts were resuspended in cold IP buffer (25 mM HEPES, 150 mM NaCl, 1 mM $MgCl_2$, 1,000 µM $CaCl_2$, 0.02% (v/v) Triton X-100 and 1× Complete Protease Inhibitor Cocktail, pH 7.1) and lysed by passing through a 1-ml syringe with a needle. The total cell lysates were centrifuged at 700 *g* for 5 min at 4 °C to remove intact cells and large cellular debris, followed by 14,000 r.p.m. centrifugation for 30 min at 4 °C. The resulting supernatant was mixed with IP buffer containing 0.08% (v/v) Triton X-100 and incubated with GFP-Trap beads (ChromoTek) at 4 °C on a rotator for 4 h, followed by 5 washes in cold washing buffer containing 0.05% (v/v) Triton X-100. Subsequently, the samples were boiled in 1× SDS sample loading buffer.

For immunoblotting, the protein samples were separated on 12% (w/v) SDS–PAGE gels and transferred to nitrocellulose membranes (Bio-Rad). The membranes were blocked in PBST with 5% (w/v) milk, followed by incubation with appropriate antibodies. Clarity Western ECL substrate solutions (Bio-Rad) were utilized to visualize luminescence. The uncropped western blot images used in this paper are provided as Source data files.

Antibodies

The primary antibodies, anti-actin (Biodragon, B1051), anti-NBR1 (Agrisera, AS14 2805), anti-cFBPase (Agrisera, AS04 043), anti-Myc (ABclonal, AE070), anti-GFP (Biodragon, B1025) and anti-ATG8 (ABclonal, A22294) were purchased from commercial companies. The anti-VSR antibodies were prepared using a truncated Arabidopsis VSR1 recombinant protein (lacking TMD and CT) expressed in *Drosophila melanogaster* S2 cells as antigen to immunize rabbits[14,36,42].

RNA extraction and quantitative RT–PCR analysis

Total RNA was extracted from inoculated leaves using the Eastep Super RNA Extraction kit (Promega, LS1040) following manufacturer instructions. Subsequently, cDNA was synthesized using the Prime Script RT Reagent kit with gDNA Eraser (RR047A, TaKaRa). RT–qPCR assays were conducted utilizing the Bio-rad Real-Time PCR System (CFX96) and the SYBR Premix Ex *Taq* kit (RR820A, TaKaRa). The transcript level of specific genes was normalized to an endogenous reference *EF1α* (At5g60390) as indicated in the figure legends. Primer details are provided in Supplementary Table 2. Each experiment included three biological replicates.

RNA-seq analysis

For RNA-seq experiments, 4-week-old plants of both WT and *vsr* mutants were infected with *Pst* DC3000 *avrRpm1* (OD = 0.05) and total RNA was prepared from the leaves at indicated times within 6 h after inoculation. RNA-seq was performed using at least three biological replicates. Total RNA was extracted using the Eastep Super RNA Extraction kit (Promega, LS1040). Sequencing libraries were prepared with total RNA using the NEB Next Poly(A) mRNA Magnetic Isolation Module (NEB). Library quality was assessed on the Agilent Bioanalyzer 2100 system. The library preparations were then sequenced on an Illumina HiSeq 2500 platform by Novogene Bioinformatics Technology. Raw data (raw reads) in fastq format were initially processed using in-house perl scripts. Subsequently, the clean reads were analysed for quality metrics such as Q20, Q30 and GC content. Clean reads of high quality were then mapped to the Col genome using Hisat2 v.2.0.5. Gene expression levels were quantified using FPKM, which represents the expected number of fragments per kilobase of transcript sequence per million base pairs sequenced. Specifically, the gene expression levels of cargo genes and ATG family genes were selected, quantified using $\log_2$ FPKM values over time (as ratios at 0 h to a control) and presented as a heat map. Images were processed using GraphPad Prism software.

The data of the hierarchical cluster analysis and heat map indicating expression of Arabidopsis *VSR* genes in response to pathogen inoculation are from the data of the Arabidopsis Affymetrix ATH1 array after bacterial pathogen infection[98].

Microarray experiments

Seedling growth conditions and bacterial inoculation were conducted as previously described[99]. Basically, Arabidopsis were sown in Petri dishes with liquid 1/2 MS medium and grown at 22 °C with continuous light. Six-day-old seedlings were transferred to 20-ml GC vials with 6 ml liquid 1/2 MS medium (7 seedlings per vial) and maintained in a growth chamber at 22 °C with continuous light (70 μE m^{-2} s^{-1}). Twelve-day-old seedlings grown in GC vials were inoculated with *P. syringae* pv tomato DC3000 at OD_{600} 0.02 or mock. Then tissue was harvested immediately (0 h) or at indicated times (3, 6 and 12 h) after the inoculation for RNA extraction. Probes were made from the RNA samples and then hybridized to the Affymetrix GeneChip containing ~8,200 genes, following procedures provided by the manufacturer.

Quantification and statistical analysis

No predetermined statistical approaches were employed to select samples or predict outcomes. Data were omitted if the controls, either negative or positive, did not function properly. Sample numbers and the number of biological replicates for each experiment are indicated in the figure legends or accompanying text. Data are expressed as mean ± s.d. Two-tailed unpaired Student's *t*-test was used when data met criteria for parametric analysis. Differences in means were considered statistically significant at $P < 0.05$. The levels of significance are denoted as follows: $^{*}P < 0.05$, $^{**}P < 0.01$, $^{***}P < 0.001$ and $^{****}P < 0.0001$. In scenarios involving multiple comparisons, one-way analysis of variance (ANOVA) was performed, followed by Fisher's least significant difference (LSD) or Tukey's post hoc test to identify significant differences. All statistical analyses were performed using GraphPad Prism v.9.1.0 software. Each experimental procedure was independently conducted a minimum of three times to ensure reliability.

Accession numbers

The Arabidopsis Genome Initiative locus identifiers for the genes mentioned in this Article are *VSR1* (At3G52850), *VSR2* (At2G30290), *VSR3* (At2G14740), *VSR4* (At2G14720), *VSR5* (At2G34940), *VSR6* (At1G30900), *VSR7* (At4G20110), *EF1α* (At5G60390), *RD21A* (At1G47128), *RD21B* (At5G43060), *RDL1* (At4G36880), *RDL2* (At3G19400), *XCP1* (At4G35350), *XBCP3* (At1G09850), *PAP1* (At2g34080), *RD19A* (At4G39090), *RD19B* (At2G21430), *AALP* (At5G60360), *CTB2* (At1G02305), *PR3* (At3G12500), *PR4* (At3G04720), *PRX33* (At3G49110), *PRX34* (At3G49120), *PRX37* (At4G08770), *CPY* (At3G10410), *VPEγ* (At4G32940), *GRX* (At5G20500), *PEP4* (AT1G11910), *ATG1b* (AT3G53930), *ATG2* (AT3G19190), *ATG3* (AT5G61500), *ATG5* (AT5G17290), *ATG7* (AT5G45900), *ATG8e* (AT2G45170), *ATG9* (AT2G31260), *ATG10* (AT3G07525), *ATG11* (AT4G30790), *ATG12a* (AT1G54210), *ATG13a* (AT3G49590), *ATG16* (AT5G50230), *ATG18b* (AT4G30510) and *ATG101* (AT5G66930). GenBank accession numbers for effectors are *avrRpm1* (X67808.1), *avrRpt2* (L11355.1) and *avrRps4* (L43559.1).

Reporting summary

Further information on research design is available in the Nature Portfolio Reporting Summary linked to this article.

Data availability

All study data are included in the article and/or its Supplementary Information. The raw Illumina reads generated from RNA-seq experiments were deposited at NCBI Sequence Read Archive (BioProject ID: PRJNA1139386). This article does not contain datasets, code or materials in addition to those included. Source data are provided with this paper.

References

1. Zhang, H. W. et al. Two tonoplast MATE proteins function as turgor-regulating chloride channels in *Arabidopsis*. *Proc. Natl Acad. Sci. USA* **114**, E2036–E2045 (2017).
2. Cui, Y. et al. MONENSIN SENSITIVITY1 (MON1)/CALCIUM CAFFEINE ZINC SENSITIVITY1 (CCZ1)-mediated Rab7 activation regulates tapetal programmed cell death and pollen development. *Plant Physiol.* **173**, 206–218 (2017).
3. Wang, X. et al. The roles of endomembrane trafficking in plant abiotic stress responses. *J. Integr. Plant Biol.* **62**, 55–69 (2020).
4. Gu, Y. N., Zavaliev, R. & Dong, X. N. Membrane trafficking in plant immunity. *Mol. Plant* **10**, 1026–1034 (2017).
5. Zhu, D., Zhang, M., Gao, C. & Shen, J. Protein trafficking in plant cells: tools and markers. *Sci. China Life Sci.* **63**, 343–363 (2020).
6. Jamet, E., Canut, H., Boudart, G. & Pont-Lezica, R. F. Cell wall proteins: a new insight through proteomics. *Trends Plant Sci.* **11**, 33–39 (2006).
7. Kim, S. J. & Brandizzi, F. The plant secretory pathway: an essential factory for building the plant cell wall. *Plant Cell Physiol.* **55**, 687–693 (2014).
8. Robinson, D. G. & Neuhaus, J. M. Receptor-mediated sorting of soluble vacuolar proteins: myths, facts, and a new model. *J. Exp. Bot.* **67**, 4435–4449 (2016).
9. Robinson, D. G. Retromer and VSR recycling: a red herring? *Plant Physiol.* **176**, 483–484 (2018).
10. Fruholz, S., Fassler, F., Kolukisaoglu, U. & Pimpl, P. Nanobody-triggered lockdown of VSRs reveals ligand reloading in the Golgi. *Nat. Commun.* **9**, 643 (2018).
11. Kunzl, F., Fruholz, S., Fassler, F., Li, B. B. & Pimpl, P. Receptor-mediated sorting of soluble vacuolar proteins ends at the *trans*-Golgi network/early endosome. *Nat. Plants* **2**, 16017 (2016).
12. Zouhar, J., Cao, W. H., Shen, J. B. & Rojo, E. Retrograde transport in plants: circular economy in the endomembrane system. *Eur. J. Cell Biol.* **102**, 151309 (2023).
13. Wang, H., Zhuang, X. H., Hillmer, S., Robinson, D. G. & Jiang, L. W. Vacuolar sorting receptor (VSR) proteins reach the plasma membrane in germinating pollen tubes. *Mol. Plant* **4**, 845–853 (2011).
14. Shen, J. et al. An in vivo expression system for the identification of cargo proteins of vacuolar sorting receptors in *Arabidopsis* culture cells. *Plant J.* **75**, 1003–1017 (2013).
15. Shimada, T. et al. Vacuolar sorting receptor for seed storage proteins in *Arabidopsis thaliana*. *Proc. Natl Acad. Sci. USA* **100**, 16095–16100 (2003).
16. Delgadillo, M. O. et al. MTV proteins unveil ER- and microtubule-associated compartments in the plant vacuolar trafficking pathway. *Proc. Natl Acad. Sci. USA* **117**, 9884–9895 (2020).
17. Hu, S. et al. Plant ESCRT protein ALIX coordinates with retromer complex in regulating receptor-mediated sorting of soluble vacuolar proteins. *Proc. Natl Acad. Sci. USA* **119**, e2200492119 (2022).
18. Li, H. et al. A plant-unique protein BLISTER coordinates with core retromer to modulate endosomal sorting of plasma membrane and vacuolar proteins. *Proc. Natl Acad. Sci. USA* **120**, e2211258120 (2023).
19. Gao, C. et al. Dual roles of an *Arabidopsis* ESCRT component FREE1 in regulating vacuolar protein transport and autophagic degradation. *Proc. Natl Acad. Sci. USA* **112**, 1886–1891 (2015).
20. Shimada, T., Takagi, J., Ichino, T., Shirakawa, M. & Hara-Nishimura, I. Plant vacuoles. *Annu. Rev. Plant Biol.* **69**, 123–145 (2018).
21. Yamada, K., Shimada, T., Nishimura, M. & Hara-Nishimura, I. A VPE family supporting various vacuolar functions in plants. *Physiol. Plant.* **123**, 369–375 (2005).

22. Hara-Nishimura, I. & Hatsugai, N. The role of vacuole in plant cell death. *Cell Death Differ.* **18**, 1298–1304 (2011).
23. Hatsugai, N. & Hara-Nishimura, I. Two vacuole-mediated defense strategies in plants. *Plant Signal. Behav.* **5**, 1568–1570 (2010).
24. Hatsugai, N. et al. A novel membrane fusion-mediated plant immunity against bacterial pathogens. *Genes Dev.* **23**, 2496–2506 (2009).
25. Carter, C. et al. The vegetative vacuole proteorne of *Arabidopsis thaliana* reveals predicted and unexpected proteins. *Plant Cell* **16**, 3285–3303 (2004).
26. Jones, J. D. G., Staskawicz, B. J. & Dangl, J. L. The plant immune system: from discovery to deployment. *Cell* **187**, 2095–2116 (2024).
27. Leong, J. X. et al. A bacterial effector counteracts host autophagy by promoting degradation of an autophagy component. *EMBO J.* **41**, e110352 (2022).
28. Banfield, M. J. Perturbation of host ubiquitin systems by plant pathogen/pest effector proteins. *Cell. Microbiol.* **17**, 18–25 (2015).
29. Lal, N. K. et al. Phytopathogen effectors use multiple mechanisms to manipulate plant autophagy. *Cell Host Microbe* **28**, 558–571 (2020).
30. Hafrén, A. et al. Selective autophagy limits cauliflower mosaic virus infection by NBR1-mediated targeting of viral capsid protein and particles. *Proc. Natl Acad. Sci. USA* **114**, E2026–e2035 (2017).
31. Zouhar, J., Muñoz, A. & Rojo, E. Functional specialization within the vacuolar sorting receptor family: VSR1, VSR3 and VSR4 sort vacuolar storage cargo in seeds and vegetative tissues. *Plant J.* **64**, 577–588 (2010).
32. Wang, Z. Y. et al. The Arabidopsis Vacuolar Sorting Receptor1 is required for osmotic stress-induced abscisic acid biosynthesis. *Plant Physiol.* **167**, 137–152 (2015).
33. Wang, D., Weaver, N. D., Kesarwani, M. & Dong, X. N. Induction of protein secretory pathway is required for systemic acquired resistance. *Science* **308**, 1036–1040 (2005).
34. Zavaliev, R. & Dong, X. NPR1, a key immune regulator for plant survival under biotic and abiotic stresses. *Mol. Cell* **84**, 131–141 (2024).
35. Glazebrook, J., Rogers, E. E. & Ausubel, F. M. Isolation of *Arabidopsis* mutants with enhanced disease susceptibility by direct screening. *Genetics* **143**, 973–982 (1996).
36. Tse, Y. C. et al. Identification of multivesicular bodies as prevacuolar compartments in *Nicotiana tabacum* BY-2 cells. *Plant Cell* **16**, 672–693 (2004).
37. Miao, Y., Yan, P., Kim, H., Hwang, I. & Jiang, L. Localization of green fluorescent protein fusions with the seven *Arabidopsis* vacuolar sorting receptors to prevacuolar compartments in tobacco BY-2 cells. *Plant Physiol.* **142**, 945–962 (2006).
38. Cui, Y. et al. Biogenesis of plant prevacuolar multivesicular bodies. *Mol. Plant* **9**, 774–786 (2016).
39. Rojo, E. et al. VPE gamma exhibits a caspase-like activity that contributes to defense against pathogens. *Curr. Biol.* **14**, 1897–1906 (2004).
40. Zhang, B. et al. PIRIN2 stabilizes cysteine protease XCP2 and increases susceptibility to the vascular pathogen *Ralstonia solanacearum* in *Arabidopsis*. *Plant J.* **79**, 1009–1019 (2014).
41. Ahmed, S. U. et al. The plant vacuolar sorting receptor AtELP is involved in transport of NH(2)-terminal propeptide-containing vacuolar proteins in *Arabidopsis thaliana*. *J. Cell Biol.* **149**, 1335–1344 (2000).
42. Shen, J., Ding, Y., Gao, C., Rojo, E. & Jiang, L. *N*-linked glycosylation of AtVSR1 is important for vacuolar protein sorting in *Arabidopsis*. *Plant J.* **80**, 977–992 (2014).
43. Miao, Y., Li, K. Y., Li, H. Y., Yao, X. & Jiang, L. The vacuolar transport of aleurain-GFP and 2S albumin-GFP fusions is mediated by the same pre-vacuolar compartments in tobacco BY-2 and *Arabidopsis* suspension cultured cells. *Plant J.* **56**, 824–839 (2008).
44. Kim, H. et al. Homomeric interaction of AtVSR1 is essential for its function as a vacuolar sorting receptor. *Plant Physiol.* **154**, 134–148 (2010).
45. Hayashi, Y. et al. A proteinase-storing body that prepares for cell death or stresses in the epidermal cells of *Arabidopsis*. *Plant Cell Physiol.* **42**, 894–899 (2001).
46. Rojo, E., Zouhar, J., Carter, C., Kovaleva, V. & Raikhel, N. V. A unique mechanism for protein processing and degradation in *Arabidopsis thaliana*. *Proc. Natl Acad. Sci. USA* **100**, 7389–7394 (2003).
47. Richau, K. H. et al. Subclassification and biochemical analysis of plant papain-like cysteine proteases displays subfamily-specific characteristics. *Plant Physiol.* **158**, 1583–1599 (2012).
48. Misas-Villamil, J. C., van der Hoorn, R. A. & Doehlemann, G. Papain-like cysteine proteases as hubs in plant immunity. *New Phytol.* **212**, 902–907 (2016).
49. Zeng, Y. L. et al. Unique COPII component AtSar1a/AtSec23a pair is required for the distinct function of protein ER export in *Arabidopsis thaliana*. *Proc. Natl Acad. Sci. USA* **112**, 14360–14365 (2015).
50. Takeuchi, M. et al. A dominant negative mutant of sar1 GTPase inhibits protein transport from the endoplasmic reticulum to the Golgi apparatus in tobacco and *Arabidopsis* cultured cells. *Plant J.* **23**, 517–525 (2000).
51. Niemes, S. et al. Sorting of plant vacuolar proteins is initiated in the ER. *Plant J.* **62**, 601–614 (2010).
52. Kwon, Y. et al. AtCAP2 is crucial for lytic vacuole biogenesis during germination by positively regulating vacuolar protein trafficking. *Proc. Natl Acad. Sci. USA* **115**, E1675–E1683 (2018).
53. Lee, Y. et al. Functional identification of sorting receptors involved in trafficking of soluble lytic vacuolar proteins in vegetative cells of *Arabidopsis*. *Plant Physiol.* **161**, 121–133 (2013).
54. Hauck, P., Thilmony, R. & He, S. Y. A *Pseudomonas syringae* type III effector suppresses cell wall-based extracellular defense in susceptible *Arabidopsis* plants. *Proc. Natl Acad. Sci. USA* **100**, 8577–8582 (2003).
55. Jones, J. D. & Dangl, J. L. The plant immune system. *Nature* **444**, 323–329 (2006).
56. Saucet, S. B. et al. Two linked pairs of *Arabidopsis* TNL resistance genes independently confer recognition of bacterial effector AvrRps4. *Nat. Commun.* **6**, 6338 (2015).
57. Tornero, P. et al. RAR1 and NDR1 contribute quantitatively to disease resistance in *Arabidopsis*, and their relative contributions are dependent on the R gene assayed. *Plant Cell* **14**, 1005–1015 (2002).
58. Mackey, D., Belkhadir, Y., Alonso, J. M., Ecker, J. R. & Dangl, J. L. *Arabidopsis* RIN4 is a target of the type III virulence effector AvrRpt2 and modulates RPS2-mediated resistance. *Cell* **112**, 379–389 (2003).
59. Munch, D. et al. Retromer contributes to immunity-associated cell death in *Arabidopsis*. *Plant Cell* **27**, 463–479 (2015).
60. Wang, Z. P. et al. Egg cell-specific promoter-controlled CRISPR/Cas9 efficiently generates homozygous mutants for multiple target genes in *Arabidopsis* in a single generation. *Genome Biol.* **16**, 144 (2015).
61. Hunter, P. R., Craddock, C. P., Di Benedetto, S., Roberts, L. M. & Frigerio, L. Fluorescent reporter proteins for the tonoplast and the vacuolar lumen identify a single vacuolar compartment in *Arabidopsis* cells. *Plant Physiol.* **145**, 1371–1382 (2007).
62. Kriegel, A. et al. Job sharing in the endomembrane system: vacuolar acidification requires the combined activity of V-ATPase and V-PPase. *Plant Cell* **27**, 3383–3396 (2015).
63. Hofius, D. et al. Autophagic components contribute to hypersensitive cell death in *Arabidopsis*. *Cell* **137**, 773–783 (2009).

64. Minina, E. A. et al. Transcriptional stimulation of rate-limiting components of the autophagic pathway improves plant fitness. *J. Exp. Bot.* **69**, 1415–1432 (2018).
65. Jung, H. et al. *Arabidopsis* cargo receptor NBR1 mediates selective autophagy of defective proteins. *J. Exp. Biol.* **71**, 73–89 (2020).
66. Zhuang, X. H. et al. A BAR-domain protein SH3P2, which binds to phosphatidylinositol 3-phosphate and ATG8, regulates autophagosome formation in *Arabidopsis*. *Plant Cell* **25**, 4596–4615 (2013).
67. Leary, A. Y., Savage, Z., Tumtas, Y. & Bozkurt, T. O. Contrasting and emerging roles of autophagy in plant immunity. *Curr. Opin. Plant Biol.* **52**, 46–53 (2019).
68. Tamura, K. et al. Why green fluorescent fusion proteins have not been observed in the vacuoles of higher plants. *Plant J.* **35**, 545–555 (2003).
69. Oliviusson, P. et al. Plant retromer, localized to the prevacuolar compartment and microvesicles in *Arabidopsis*, may interact with vacuolar sorting receptors. *Plant Cell* **18**, 1239–1252 (2006).
70. Gershlick, D. C. et al. Golgi-dependent transport of vacuolar sorting receptors is regulated by COPII, AP1, and AP4 protein complexes in tobacco. *Plant Cell* **26**, 1308–1329 (2014).
71. Fuji, K. et al. The adaptor complex AP-4 regulates vacuolar protein sorting at the trans-Golgi network by interacting with VACUOLAR SORTING RECEPTOR1. *Plant Physiol.* **170**, 211–219 (2016).
72. Avila, E. L. et al. Expression analysis of *Arabidopsis* vacuolar sorting receptor 3 reveals a putative function in guard cells. *J. Exp. Bot.* **59**, 1149–1161 (2008).
73. Aarts, N. et al. Different requirements for EDS1 and NDR1 by disease resistance genes define at least two R gene-mediated signaling pathways in *Arabidopsis*. *Proc. Natl Acad. Sci. USA* **95**, 10306–10311 (1998).
74. Axtell, M. J. & Staskawicz, B. J. Initiation of RPS2-specified disease resistance in *Arabidopsis* is coupled to the AvrRpt2-directed elimination of RIN4. *Cell* **112**, 369–377 (2003).
75. van Doorn, W. G. Classes of programmed cell death in plants, compared to those in animals. *J. Exp. Bot.* **62**, 4749–4761 (2011).
76. Happel, N. et al. *Arabidopsis* mu A-adaptin interacts with the tyrosine motif of the vacuolar sorting receptor VSR-PS1. *Plant J.* **37**, 678–693 (2004).
77. Hatsugai, N. et al. Involvement of adapter protein complex 4 in hypersensitive cell death induced by avirulent bacteria. *Plant Physiol.* **176**, 1824–1834 (2018).
78. Marquardt, L. et al. Vacuole fragmentation depends on a novel Atg18-containing retromer-complex. *Autophagy* **19**, 278–295 (2023).
79. Zavodszky, E. et al. Mutation in VPS35 associated with Parkinson's disease impairs WASH complex association and inhibits autophagy. *Nat. Commun.* **5**, 3828 (2014).
80. Boutouja, F. et al. Vps10-mediated targeting of Pep4 determines the activity of the vacuole in a substrate-dependent manner. *Sci. Rep.* **9**, 10557 (2019).
81. Üstün, S., Hafrén, A. & Hofius, D. Autophagy as a mediator of life and death in plants. *Curr. Opin. Plant Biol.* **40**, 122–130 (2017).
82. Üstün, S. & Hofius, D. Anti- and pro-microbial roles of autophagy in plant–bacteria interactions. *Autophagy* **14**, 1465–1466 (2018).
83. Yuan, M. et al. Pattern-recognition receptors are required for NLR-mediated plant immunity. *Nature* **592**, 105–109 (2021).
84. Lenz, H. D. et al. Autophagy differentially controls plant basal immunity to biotrophic and necrotrophic pathogens. *Plant J.* **66**, 818–830 (2011).
85. Mohr, P. G. & Cahill, D. M. Suppression by ABA of salicylic acid and lignin accumulation and the expression of multiple genes, in *Arabidopsis* infected with *Pseudomonas syringae* pv. tomato. *Funct. Integr. Genomics* **7**, 181–191 (2007).
86. O'Brien, J. A., Daudi, A., Butt, V. S. & Bolwell, G. P. Reactive oxygen species and their role in plant defence and cell wall metabolism. *Planta* **236**, 765–779 (2012).
87. Schlößer, M. et al. Localization of four class I glutaredoxins in the cytosol and the secretory pathway and characterization of their biochemical diversification. *Plant J.* **118**, 1455–1474 (2024).
88. Koestel, J. & Batoko, H. A plant-specific bridging adaptor for amphisome biogenesis. *J. Cell Biol.* **221**, e202210011 (2022).
89. Hu, S., Li, Y. & Shen, J. A diverse membrane interaction network for plant multivesicular bodies: roles in proteins vacuolar delivery and unconventional secretion. *Front. Plant Sci.* **11**, 425 (2020).
90. Shen, J. et al. A plant Bro1 domain protein BRAF regulates multivesicular body biogenesis and membrane protein homeostasis. *Nat. Commun.* **9**, 3784 (2018).
91. Ohad, N., Shichrur, K. & Yalovsky, S. The analysis of protein–protein interactions in plants by bimolecular fluorescence complementation. *Plant Physiol.* **145**, 1090–1099 (2007).
92. Krebs, M. et al. *Arabidopsis* V-ATPase activity at the tonoplast is required for efficient nutrient storage but not for sodium accumulation. *Proc. Natl Acad. Sci. USA* **107**, 3251–3256 (2010).
93. Grant, M. R. et al. Structure of the *Arabidopsis* RPM1 gene enabling dual specificity disease resistance. *Science* **269**, 843–846 (1995).
94. Mindrinos, M., Katagiri, F., Yu, G. L. & Ausubel, F. M. The *A. thaliana* disease resistance gene RPS2 encodes a protein containing a nucleotide-binding site and leucine-rich repeats. *Cell* **78**, 1089–1099 (1994).
95. Wirthmueller, L., Zhang, Y., Jones, J. D. & Parker, J. E. Nuclear accumulation of the *Arabidopsis* immune receptor RPS4 is necessary for triggering EDS1-dependent defense. *Curr. Biol.* **17**, 2023–2029 (2007).
96. Miao, Y. & Jiang, L. Transient expression of fluorescent fusion proteins in protoplasts of suspension cultured cells. *Nat. Protoc.* **2**, 2348–2353 (2007).
97. Shen, J. et al. AtBRO1 functions in ESCRT-I complex to regulate multivesicular body protein sorting. *Mol. Plant* **9**, 760–763 (2016).
98. Wang, L. et al. The genetic network controlling the *Arabidopsis* transcriptional response to *Pseudomonas syringae* pv. maculicola: roles of major regulators and the phytotoxin coronatine. *Mol. Plant Microbe Interact.* **21**, 1408–1420 (2008).
99. Guan, R. et al. Multilayered regulation of ethylene induction plays a positive role in *Arabidopsis* resistance against *Pseudomonas syringae*. *Plant Physiol.* **169**, 299–312 (2015).

Acknowledgements

We thank Y. Xia (Hong Kong Baptist University) for providing *Pto* DC3000 expressing *avrRpm1* or *avrRps4*, and *Pto* DC3000 *hrcC*$^-$ strain; Y. Liang (Zhejiang University) for providing the *rpm1* mutant plant; Y. Xiang (Lanzhou University) for providing the *vha-a2 vha-a3* double mutant plant; Q.-J. Chen (China Agricultural University) for providing the CRISPR-Cas9 system; R. W. Innes (Indiana University) for providing the pTA7002-DEX backbone; X. Deng for the initial pathology tests; and S. Zhang (University of Missouri) for insightful suggestions and technical advice. This work was supported by grants from the National Natural Science Foundation of China (32170342 and 31970181), the Zhejiang Provincial Natural Science Foundation of China (LR20C020001), the Zhejiang A&F University Starting Funding (2024LFR053), and the 111 Project (D18008) to J.S.; the National Natural Science Foundation of China (32100286) to S.H.; and the Spanish Ministry for Science and Innovation MCIN/AEI/10.13039/501100011033/FEDER grant PID2021-128078NB-I00 to E.R.

Author contributions

J.S., S.H. and E.R. designed the research. D.Z., S.H., W.C., Y.G., Y.L. and B.L. performed experiments. D.Z., S.H., E.R., J.X., L.J. and J.S. analysed the data. Y.G., Y.L. and B.L. contributed to material preparation. J.S., E.R. and L.J. wrote the paper with comments from all authors.

Competing interests

The authors declare no competing interests.

Additional information

Extended data is available for this paper at https://doi.org/10.1038/s41477-025-02077-8.

Supplementary information The online version contains supplementary material available at https://doi.org/10.1038/s41477-025-02077-8.

Correspondence and requests for materials should be addressed to Jinbo Shen.

Peer review information *Nature Plants* thanks Takashi Ueda and the other, anonymous, reviewer(s) for their contribution to the peer review of this work.

https://doi.org/10.1038/s41477-025-02077-8

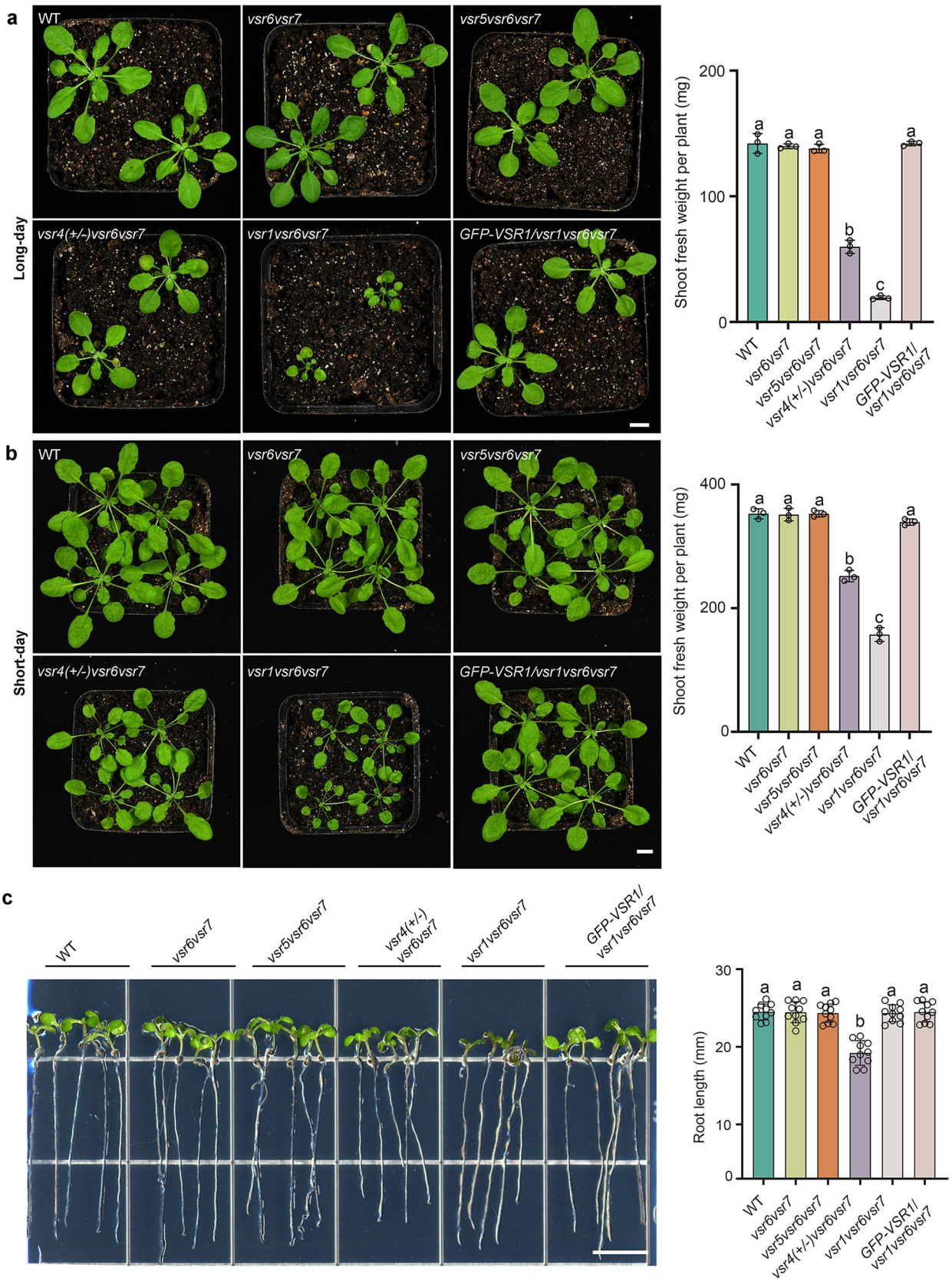

Extended Data Fig. 1 | See next page for caption.

https://doi.org/10.1038/s41477-025-02077-8

Extended Data Fig. 1 | Phenotype analysis of different *vsr* mutant combinations. (**a and b**) Phenotype of 24-day-old plants grown under long-day (**a**) or short-day (**b**) growth condition of the indicated *vsr* mutants and complemented lines with indicated GFP fusions. Note that homozygous *vsr4vsr6vsr7* triple mutant are not identified from the self-pollination of *vsr4(+/-) vsr6vsr7*. All photographs are at the same magnification. The wet weights of shoot per plant of the indicated genotypes were quantified (*Right*). Data are presented as means ± SD from three independent experiments. Scale bar, 1 cm. (**c**) Seven-day-old seedlings of indicated genotypes were photographed. The root length of seedlings of the indicated genotypes was quantified (*Right*). Data are presented as means ± SD of 10 seedlings from three independent experiments. Scale bar, 1 cm. Different letters above bars in (**a**-**c**) indicate a significant difference at the $P < 0.05$ level by one-way ANOVA with Fisher's LSD multiple comparisons test. Exact *P*-values of statistic tests in (**a**-**c**) are provided in the Source data file.

https://doi.org/10.1038/s41477-025-02077-8

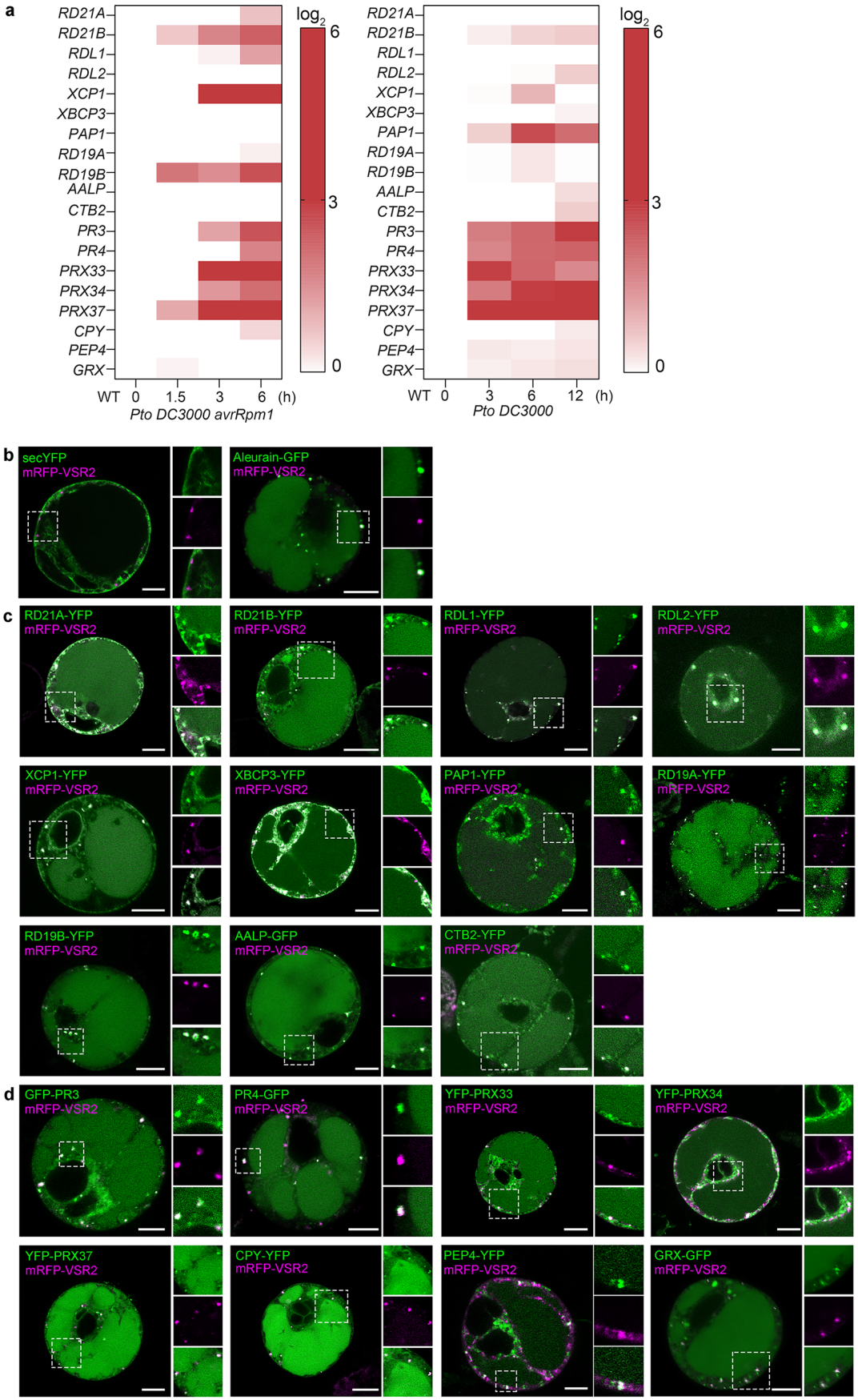

Extended Data Fig. 2 | See next page for caption.

https://doi.org/10.1038/s41477-025-02077-8

Extended Data Fig. 2 | Vacuolar localization of pathogen upregulated proteins as putative VSR cargo proteins. **(a)** Transcript levels (log_2) of genes, function as putative VSR cargo proteins, in WT plants after inoculation of the *Pto* DC3000 *avrRpm1* or *Pto* DC3000 at indicated time of post inoculation. Heatmap displays the relative expression (log_2FC) of the genes in WT plants after inoculation with *Pto* DC3000 *avrRpm1* or *Pto* DC3000 at different times points after inoculation relative to their expression before inoculation (0 h). **(b)** Subcellular localization of secYFP and Aleurain-GFP as controls. secYFP showed ER pattern, without any fluorescence signal in the vacuole. Vacuolar localized protein Aleurain-GFP colocalized with the PVC/MVB marker mRFP-VSR2 in punctae and showed diffused fluorescence signals in vacuole. Separated images of each channel in the white outline area are shown on the right side (from top to bottom: GFP/YFP, mRFP, and merged). Scale bars, 10 μm. **(c)** Colocalization of GFP/YFP-tagged putative VSR cargo in Papain-Like Cysteine Proteases family with the PVC/MVB marker mRFP-VSR2 was analyzed with a confocal microscope in protoplasts of Arabidopsis suspension cells. Separated images of each channel in the white outline area are shown on the right side (from top to bottom: GFP/YFP, mRFP, and merged). Scale bars, 10 μm. **(d)** Subcellular localization analysis of two Pathogenesis-related proteins (PR3 and PR4), three peroxidases (PRX33, PRX34, and PRX37), CPY, PEP4, and GRX. Colocalization of GFP/YFP-tagged proteins with the PVC/MVB marker mRFP-VSR2 was analyzed with a confocal microscope in protoplasts of Arabidopsis suspension cells. Separated images of each channel in the white outline area are shown on the right side (from top to bottom: GFP/YFP, mRFP, and merged). Scale bars, 10 μm. Similar confocal imaging results to those in (**b**–**d**) were obtained from three independent experiments.

https://doi.org/10.1038/s41477-025-02077-8

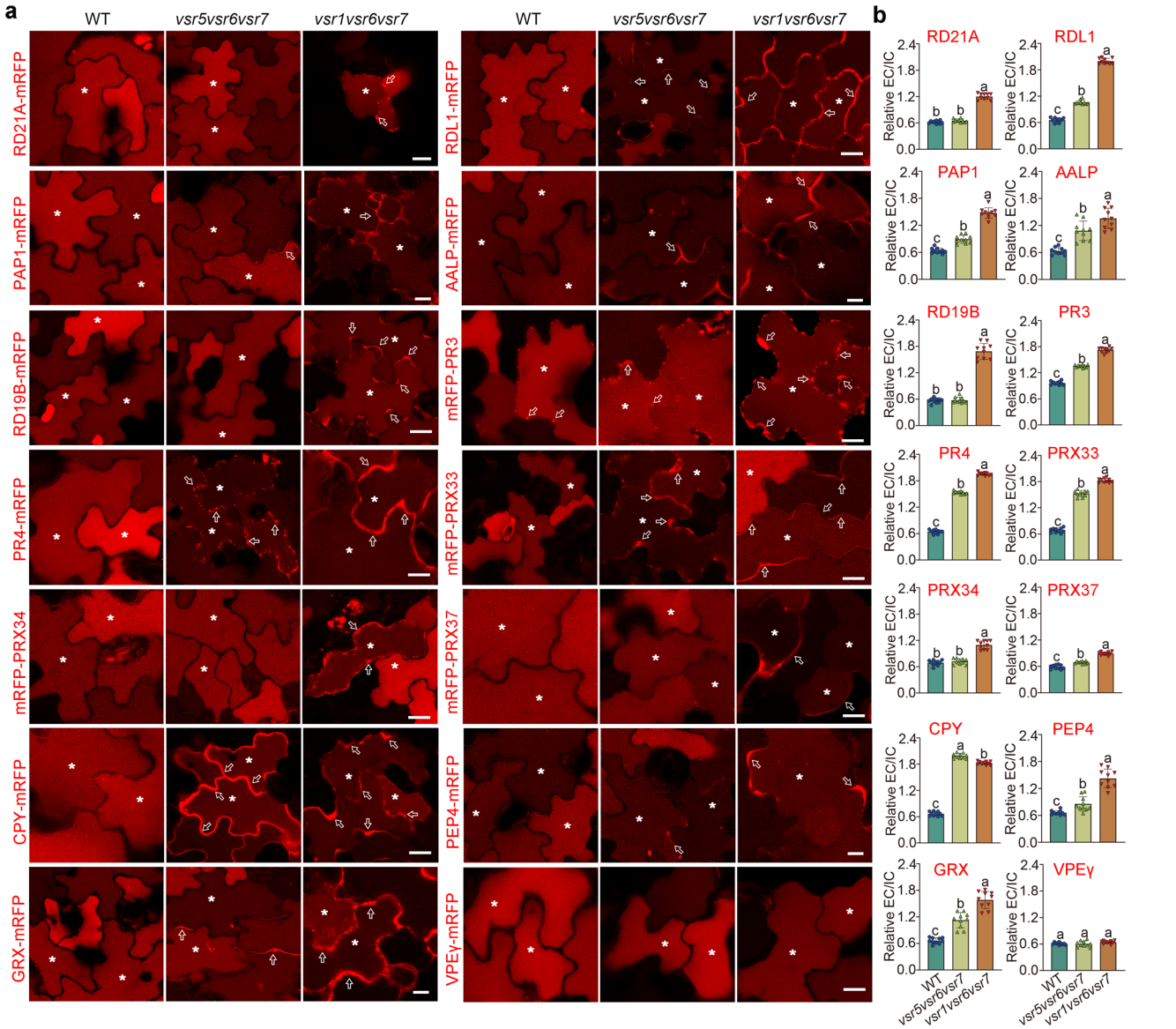

Extended Data Fig. 3 | Extracellular localization of pathogen-induced VSR cargo proteins in *vsr* mutants. **(a)** Confocal images of cotyledon cells from Arabidopsis seedlings of the indicated genotypes transiently transformed with RD21A-mRFP, RDL1-mRFP, PAP1-mRFP, AALP-mRFP, RD19B-mRFP, mRFP-PR3, PR4-mRFP, mRFP-PRX33, mRFP-PRX34, mRFP-PRX37, CPY-mRFP, PEP4-mRFP, and GRX-mRFP. Arrows and asterisks indicate the fluorescence signal in extracellular spaces and vacuoles, respectively. Note that in the *vsr5vsr6vsr7* or *vsr1vsr6vsr7* triple mutants, much stronger fluorescent signal in the extracellular space (arrows), compared to that in WT. The vacuole protein VPEγ-RFP was not secreted in *vsr* mutant cells, suggesting the specificity of VSR sorting. Scale bar, 10 μm. **(b)** Quantification of relative extracellular (EC) to intracellular (IC) fluorescence intensity values for the indicated RFP tagged proteins. The region of interest (ROI) was kept constant for each measurement. Data are presented as means ± SD of 10 cells from three independent experiments. Different letters above bars indicate a significant difference at the $P < 0.05$ level by one-way ANOVA with Fisher's LSD multiple comparisons test. Exact *P*-values of statistic tests are provided in the Source data file.

https://doi.org/10.1038/s41477-025-02077-8

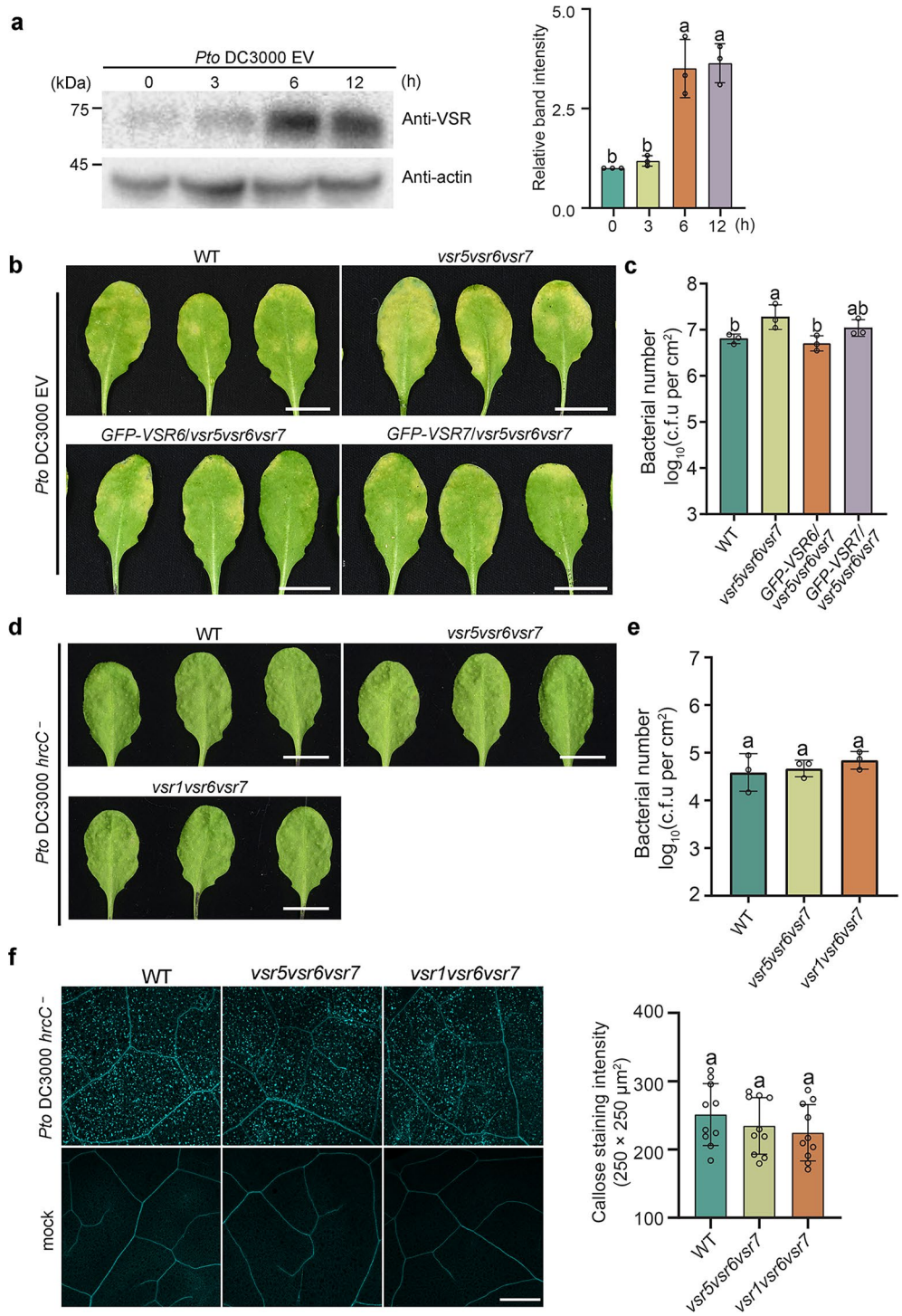

Extended Data Fig. 4 | VSRs are weakly involved in PTI. (**a**) VSR proteins level after inoculation with virulent strains *Pto* DC3000 EV. Seedlings of WT plants after inoculation with virulent strains of *Pto* DC3000 EV (OD_{600} = 0.02) at the indicated time points (0, 3, 6, and 12 h) were applied for protein extraction and immunoblotting with anti-VSR antibodies. The anti-actin was used as a loading control. The VSR protein level in the immunoblot was quantified (*Right*). Intensity was normalized by the loading control of anti-actin, and the first lane (0 h) in each experiment was arbitrarily set to 1. Data are presented as means ± SD from three independent experiments. (**b**) Disease symptoms on representative infected leaves. Leaves of indicated genotype plants 3 d after inoculation with *Pto* DC3000 EV (OD_{600} = 0.001). Leaves of *vsr5vsr6vsr7* triple mutant inoculated exhibit chlorotic symptoms. Scale bars, 1 cm. (**c**) Bacterial growth 3 d after inoculation with *Pto* DC3000 EV (OD_{600} = 0.001) in the leaves of indicated genotype plants. Each bar represents log_{10}-transformed values of the mean and SD of three biological replicates. Experiments were repeated three times with similar results. (**d**) Disease symptoms on representative infected leaves. Leaves of indicated genotype plants 3 d after inoculation with *Pto* DC3000 *hrcC*$^-$ (OD_{600} = 0.001). Scale bars, 1 cm. (**e**) Bacterial growth 3 d after inoculation with *Pto* DC3000 *hrcC*$^-$ (OD_{600} = 0.001) in the leaves of indicated genotype plants. Each bar represents log_{10}-transformed values of the mean and SD of three biological replicates. c.f.u., colony-forming units. (**f**) Callose deposition in leaves of the indicated plant lines inoculated with *Pto* DC3000 *hrcC*$^-$ (OD600 = 0.1) and water (mock) detected by aniline blue staining at 12 h after inoculation. Quantification of callose staining intensity is shown on *Right*. Data are presented as means ± SD of 10 stained regions from three independent repeats. Scale bar, 500 μm. Different letters above bars in (**a, c, e** and **f**) indicate a significant difference at the $P < 0.05$ level by one-way ANOVA with Fisher's LSD multiple comparisons test. Exact *P*-values of statistic tests in (**a, c, e,** and **f**) are provided in the Source data file.

https://doi.org/10.1038/s41477-025-02077-8

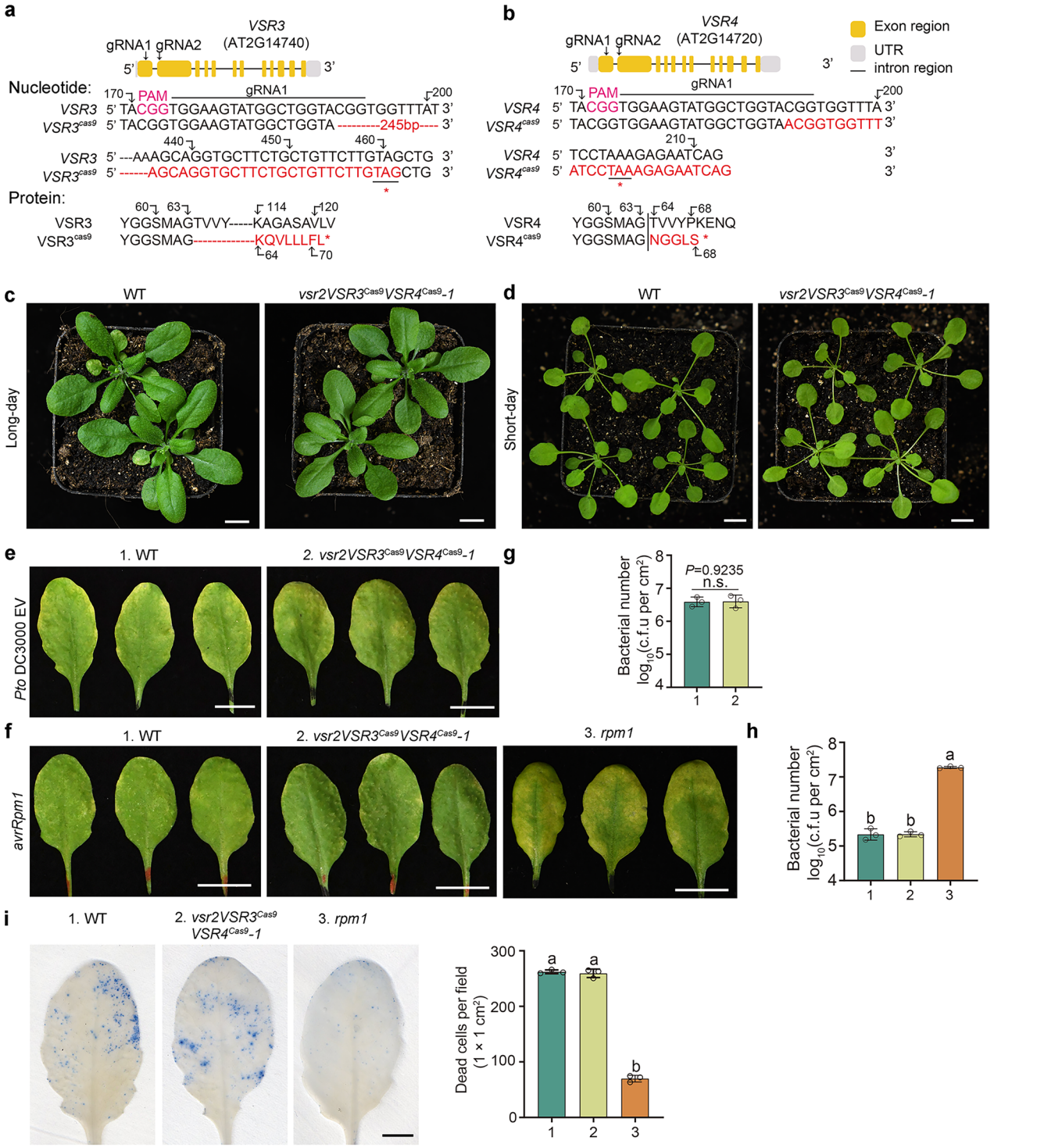

Extended Data Fig. 5 | Phenotype analysis of *vsr2VSR3*^{Cas9}*VSR4*^{Cas9}*-1* mutant. (**a** and **b**) Sequencing analysis of CRISPR-Cas9 edited line of *vsr2VSR3*^{Cas9} *VSR4*^{Cas9}*-1*. CRISPR-Cas9 editing of *VSR3* (**a**) and *VSR4* (**b**) was carried out using *vsr2* T-DNA insertion mutant as the background. *VSR3* and *VSR4* share closely related sequences thus with identical gRNA1 and gRNA2 targets. Below each gene model, the nucleotide sequences are shown alongside the corresponding amino acid translations. The nucleotides highlighted in red in the sequences are specific changes from WT sequences. The stop codes are marked with stars. (**c** and **d**) Phenotype of 24-day-old plants grown under long-day (**c**) or short-day (**d**) growth condition. The experiments were repeated independently three times with similar results. (**e** and **f**) Disease symptoms analysis of *vsr2VSR3*^{Cas9}*VSR4*^{Cas9}*-1* mutant. Leaves of WT and *vsr2VSR3*^{Cas9}*VSR4*^{Cas9}*-1* triple mutant after 3 d inoculation with the *Pto* DC3000 EV (**e**) or *Pto* DC3000 expressing *avrRpm1* (OD_{600} = 0.001) (**f**). Loss-of-function mutant of the corresponding resistance gene *RPM1* (*rpm1*) served as an additional control. Scale bars, 1 cm. (**g** and **h**) Bacterial growth 3 d after inoculation with *Pto* DC3000 expressing *Pto* DC3000 EV (**g**) or *avrRpm1* (**h**) in the leaves. Each bar represents log_{10}-transformed values of the mean and SD of three biological replicates. Experiments were repeated three times with similar results. cfu, colony-forming units. (**i**) Trypan blue staining of dead cells in the leaves of WT, *vsr2VSR3*^{Cas9}*VSR4*^{Cas9}*-1*, and *rpm1* mutants at 12 h after inoculation with *Pto* DC3000 *avrRpm1* (OD_{600} = 0.001). Quantifications of trypan blue staining intensity are shown on the *Right*. Data are presented as means ± SD of three independent experiments. Scale bars, 5 mm. Different letters above bars in (**g**-**i**) indicate a significant difference at the $P < 0.05$ level by one-way ANOVA with Fisher's LSD multiple comparisons test. Exact *P*-values of statistic tests in (**h** and **i**) are provided in the Source data file.

https://doi.org/10.1038/s41477-025-02077-8

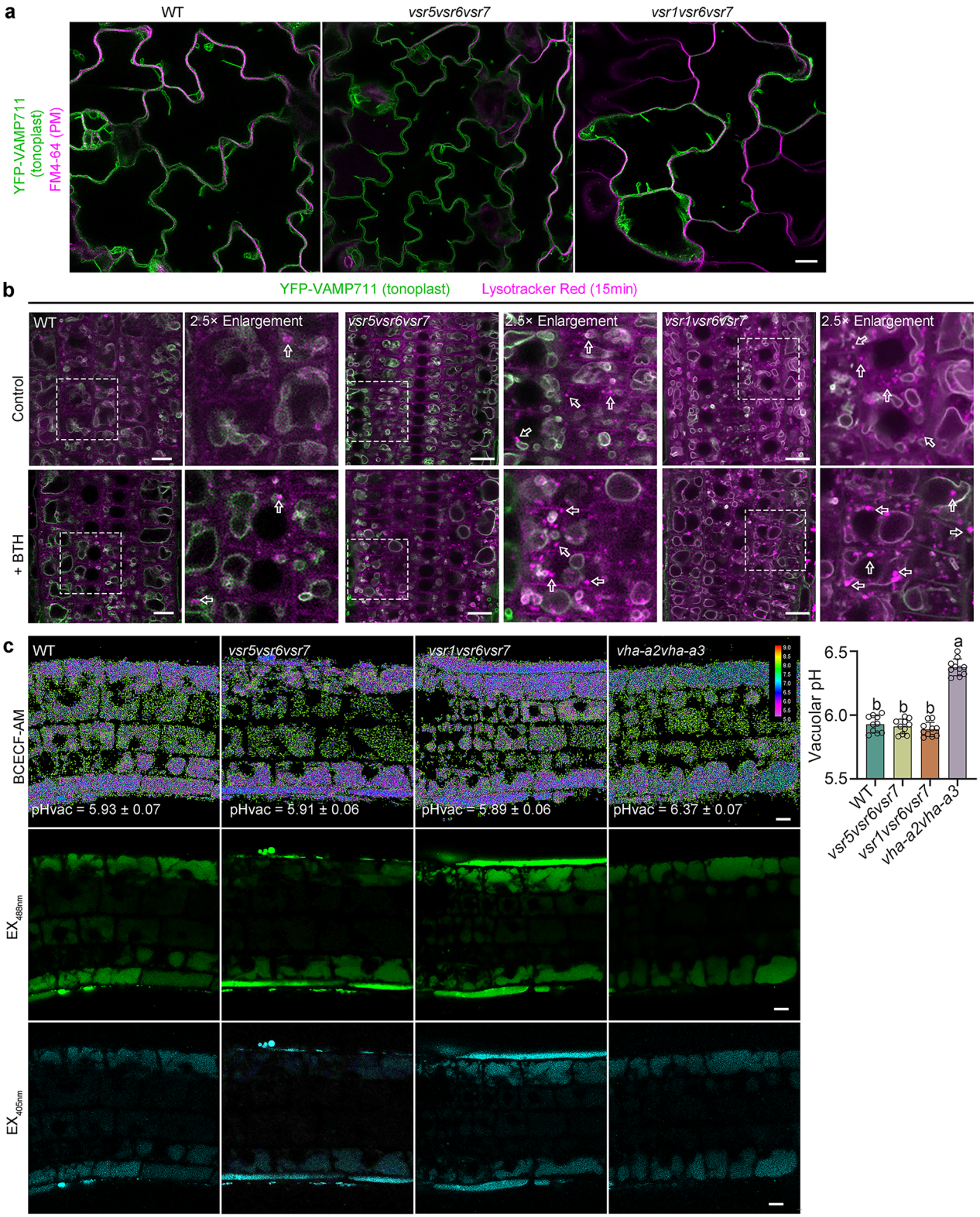

Extended Data Fig. 6 | See next page for caption.

https://doi.org/10.1038/s41477-025-02077-8

Extended Data Fig. 6 | Vacuole morphology and vacuolar pH analysis in *vsr* mutants. (**a**) Confocal microscopic images of the vacuolar membrane marker YFP-VAMP711 expressed in leaf epidermal cells of WT and *vsr* mutants. FM4-64 was used to label and visualize the cell PM. No obvious vacuole fragmentation was observed in leaf cells of the indicated *vsr* mutants. Scale bar, 10 μm. (**b**) Lysotracker Red staining indicates aberrant aggregation (arrows) of lytic compartments in root cells of *vsr5vsr6vsr7* and *vsr1vsr6vsr7* mutants in comparison with WT plants (*Top*). The morphological phenotype was further aggravated in *vsr5vsr6vsr7* and *vsr1vsr6vsr7* upon treatment with 100 μM BTH (bottom). Control and BTH-treated 5-d-old seedlings were stained with 2 μM Lysotracker Red for 15 min before imaging. The green signals of YFP-VAMP711 show the tonoplast. Imaging conditions were identical across all genotypes. Scale bar, 10 μm. (**c**) The pH of vacuole is not altered in *vsr* mutants. Representative pseudo-colored images of the vacuole in WT, *vsr5vsr6vsr7*, and *vsr1vsr6vsr7*. The rainbow scale correlates to pH value. The vacuolar H^+-ATPase mutant *vha-a2 vha-a3* was used as a control. Quantification of vacuole pH (*Right*). Compared to WT, no significant difference ($P > 0.05$) in vacuole pH in *vsr5vsr6vsr7* or *vsr1vsr6vsr7* mutant, while loss of the tonoplast VATPase increases the vacuolar pH in root epidermal cells. Data are presented as means ± SD of 10 seedlings from three independent experiments. Different letters above bars indicate a significant difference at the $P < 0.05$ level by one-way ANOVA with Fisher's LSD multiple comparisons test. Scale bar, 10 μm. Similar confocal imaging results to those in (**a** and **b**) were obtained from three independent experiments. Exact *P*-values of statistic tests are provided in the Source data file.

https://doi.org/10.1038/s41477-025-02077-8

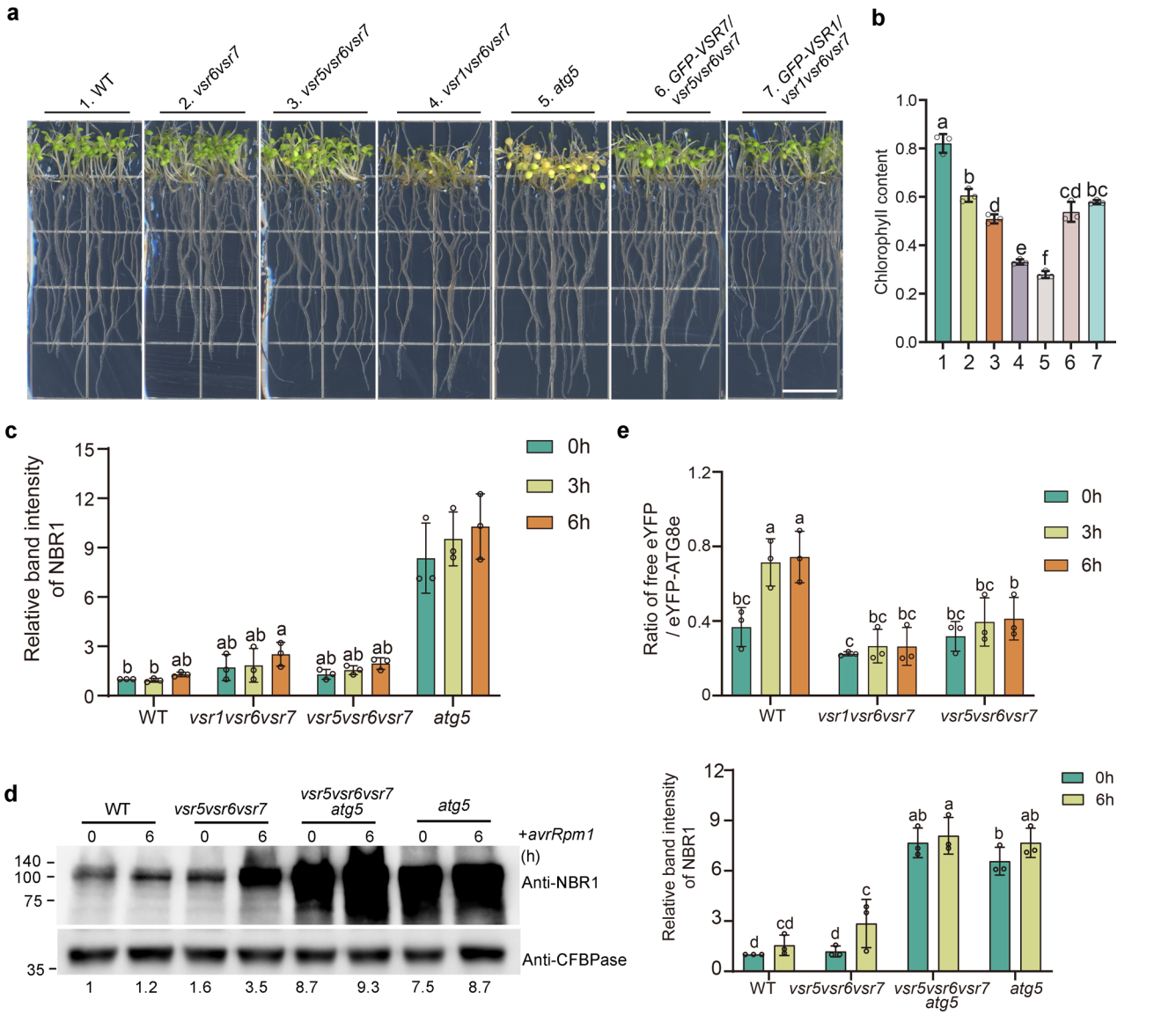

Extended Data Fig. 7 | Autophagic phenotype analysis of *vsr* mutants. (**a**) Photographs of the seedlings from the indicated genotypes after maintaining them for 7 d in complete darkness. Seedlings were grown 7 d on half-strength MS under long-day conditions before transfer to dark. Note that starvation-induced chlorosis is enhanced in *vsr5vsr6vsr7* or *vsr1vsr6vsr7*, compared with WT or complemented lines (*GFP-VSR7/vsr5vsr6vsr7* and *GFP-VSR1/vsr1vsr6vsr7*). Scale bar, 1 cm. (**b**) Quantification analysis of the total chlorophyll content of seedlings in (**a**). Data are presented as means ± SD of three independent experiments. (**c**) Quantification analysis of the NBR1 proteins level upon infection with *Pto* DC3000 *avrRpm1*. The immunoblot intensity was normalized by the loading control of anti-actin, and the first lane (0 h) in each experiment was arbitrarily set to 1. Data are presented as means ± SD from three independent experiments. The differences were compared among WT and *vsr* mutants at the indicated time points. (**d**) Immunoblot analysis of NBR1 accumulation upon infection with *Pto* DC3000 *avrRpm1*. Total proteins were extracted from 5-day-old WT, *vsr5vsr6vsr7*, *vsr5vsr6vsr7atg5*, and *atg5* seedlings at the indicated time points (0 and 6 h), followed by immunoblot analysis with anti-NBR1 antibody. The cytoplasmic marker anti-cFBPase is used as a loading control. The immunoblot intensity was normalized by the loading control of anti-cFBPase, and the first lane (WT, 0 h) was arbitrarily set to 1. Quantification analysis of the NBR1 proteins level is shown on *Right*. Data are presented as means ± SD from three independent experiments. (**e**) Quantification analysis of the ratio of free eYFP to eYFP-ATG8e proteins level upon infection with *Pto* DC3000 *avrRpm1*. Data are presented as means ± SD from three independent experiments. Different letters above bars indicate a significant difference at the $P < 0.05$ level by one-way ANOVA with Fisher's LSD (**b, d,** and **e**) or Tukey's (**c**) multiple comparisons test. Exact *P*-values of statistic tests in (**b**-**e**) are provided in the Source data file.

https://doi.org/10.1038/s41477-025-02077-8

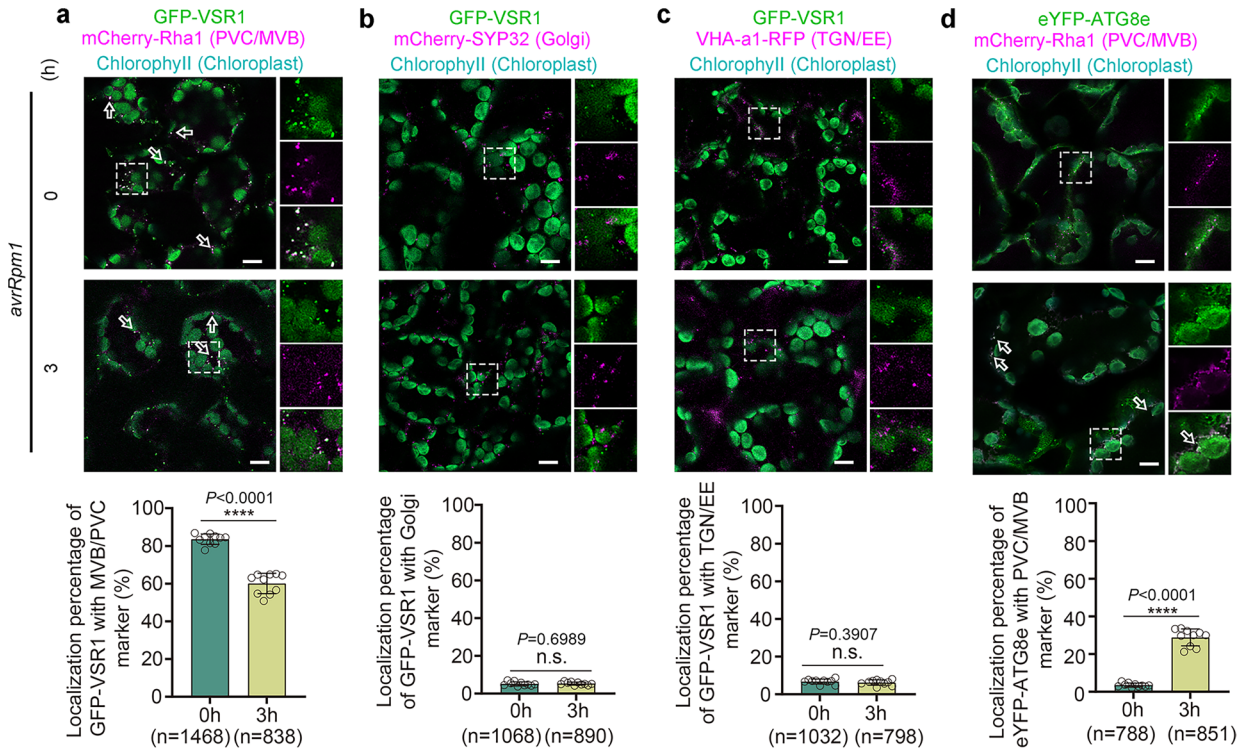

Extended Data Fig. 8 | Colocalization analysis of GFP-VSR1 with endosomal markers after infection with *Pto* DC3000 *avrRpm1*. (**a-c**) Colocalization analysis of GFP-VSR1 with the MVB/PVC marker mCherry-Rha1 (**a**), Golgi marker mCherry-SYP32 (**b**), and TGN marker VHA-a1-RFP (**c**). Confocal images are representative of mesophyll cells in leaves of 4-week-old plants before (0) and after (3 h) inoculation of the *Pto* DC3000 *avrRpm1*. (**d**) Colocalization analysis of mCherry-Rha1 with the autophagosome marker eYFP-ATG8e in leaves of 4-week-old plants before (0) and after (3 h) inoculation of the *Pto* DC3000 *avrRpm1*. Separated images of each channel in the white outlined area are shown on the right side (from top to bottom: GFP/eYFP, RFP/mCherry, and merged). Arrows indicate the colocalized fluorescence. The colocalization percentage is included in the bottom. Colocalization was quantified from 10 individual leaves of three independent experiments. Data are presented as means ± SD. n, total numbers of analyzed punctae. ****$P < 0.0001$; n.s., $P > 0.05$ in two-tailed unpaired Student's *t*-test. Scale bars, 10 μm.

https://doi.org/10.1038/s41477-025-02077-8

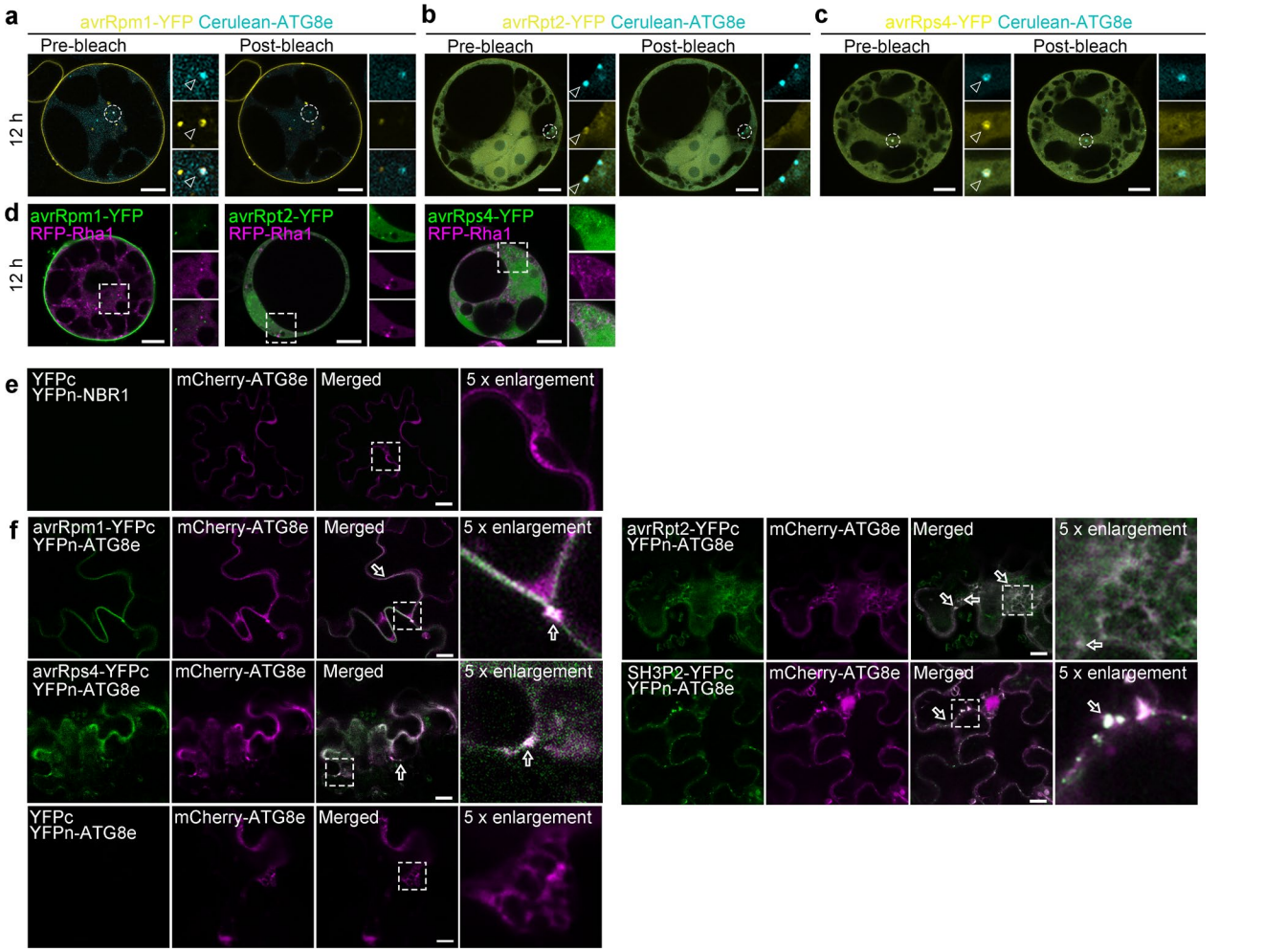

Extended Data Fig. 9 | Effector proteins colocalized and interacted with ATG8. (**a**-**c**) FRET analysis of the colocalized puncta between YFP tagged avrRpm1-YFP (**a**), avrRpt2-YFP (**b**), or avrRps4-YFP (**c**) and cerulean tagged ATG8e in protoplasts of Arabidopsis suspension cells. The dashed circular outlines indicate examples of colocalized punctae for photobleaching. Arrows indicate the colocalized fluorescence. Separated images of each channel, both pre-bleach and post-bleach, are shown on the right side (from top to bottom: CFP, YFP, and merged). Scale bars, 10 μm. (**d**) Colocalization analysis of avrRpm1-YFP, avrRpt2-YFP, or avrRps4-YFP with the PVC/MVB marker RFP-Rha1 in protoplasts of Arabidopsis suspension cells. Separated images of each channel are shown on the right side (from top to bottom: YFP, RFP, and merged). Scale bars, 10 μm. (**e**) The pair of YFPc and YFPn-NBR1 was used as a negative control for NBR1 interaction with avrRpm1, avrRpt2, and avrRps4 in *N. benthamiana* plants using a BiFC assay. (**f**) ATG8e interaction with bacterial effectors avrRpm1, avrRpt2, and avrRps4 in *N. benthamiana* plants using a BiFC assay. ATG8e fused with a N-terminus of YFP (YFPn) was co-expressed with avrRpm1, avrRpt2, or avrRps4 fused with C-terminus YFP (YFPc). Reconstituted YFP fluorescence, colocalized with autophagosome marker mCherry-ATG8e, indicates a positive interaction. The pair of SH3P2-YFPc and YFPn- ATG8e was used as a positive control, while the pair of YFPc and YFPn-ATG8e was used as a negative control. The regions within the white outline are enlarged (*Right*) (magnification: 5×). Scale bar, 10 μm. The experiments in (**d**–**f**) were repeated independently three times with similar results.

https://doi.org/10.1038/s41477-025-02077-8

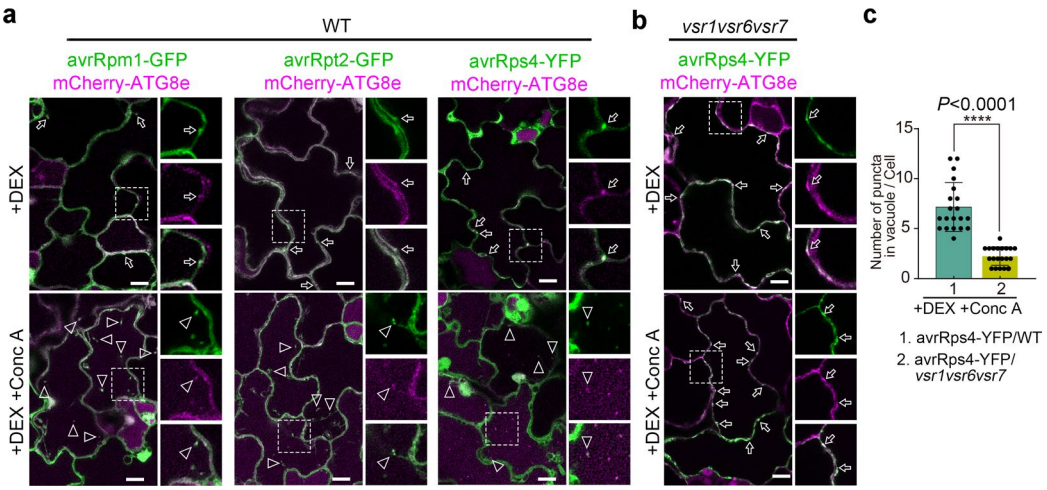

Extended Data Fig. 10 | The autophagic degradation of effectors was impaired in *vsr* mutant plant. **(a)** Colocalization analysis of GFP/YFP fused effectors and mCherry-ATG8e. Five-day-old transgenic plants expressing autophagosome marker mCherry-ATG8e and the *DEX::avrRpm1-GFP*, *DEX::avrRpt2-GFP*, or *DEX::avrRps4-YFP* were treated with DEX (+) for 24 h, with (+) or without 0.5 μM Conc A for 6 h, followed by confocal analysis. The regions within the white outline are enlarged. Arrows and arrowheads indicate colocalized punctae in cytosol or vacuole, respectively. Scale bar, 10 μm. **(b)** *VSR* mutant impair the autophagy degradation of avrRps4-YFP. Confocal images of cotyledon cells from Arabidopsis seedlings of the *vsr1vsr6vsr7* transformed with *DEX::avrRps4-YFP* after DEX induction for 24 h, with (+) or without 0.5 μM Conc A for 6 h, followed by confocal analysis. Note that the *vsr1vsr6vsr7* triple mutants accumulated YFP and mCherry positive puncta (arrows) in the cytosol after ConcA treatment, whereas WT Conc A treated plants displayed mostly intravacuolar localization of the puncta (arrowheads). Scale bar, 10 μm. **(c)** Quantification of the number of avrRps4-YFP punctae in vacuole when plants were treated with DEX (+) and Conc A (+). Data are presented as means ± SD of 20 individual cells from three independent experiments. ****$P < 0.0001$ in two-tailed unpaired Student's *t*-test. Scale bars, 10 μm. The experiments in (**a** and **b**) were repeated independently three times with similar results.

nature portfolio

Corresponding author(s): Jinbo Shen

Last updated by author(s): Jul 1, 2025

Reporting Summary

Nature Portfolio wishes to improve the reproducibility of the work that we publish. This form provides structure for consistency and transparency in reporting. For further information on Nature Portfolio policies, see our Editorial Policies and the Editorial Policy Checklist.

Statistics

For all statistical analyses, confirm that the following items are present in the figure legend, table legend, main text, or Methods section.

n/a	Confirmed	
☐	☒	The exact sample size (*n*) for each experimental group/condition, given as a discrete number and unit of measurement
☐	☒	A statement on whether measurements were taken from distinct samples or whether the same sample was measured repeatedly
☐	☒	The statistical test(s) used AND whether they are one- or two-sided *Only common tests should be described solely by name; describe more complex techniques in the Methods section.*
☒	☐	A description of all covariates tested
☐	☒	A description of any assumptions or corrections, such as tests of normality and adjustment for multiple comparisons
☐	☒	A full description of the statistical parameters including central tendency (e.g. means) or other basic estimates (e.g. regression coefficient) AND variation (e.g. standard deviation) or associated estimates of uncertainty (e.g. confidence intervals)
☐	☒	For null hypothesis testing, the test statistic (e.g. *F*, *t*, *r*) with confidence intervals, effect sizes, degrees of freedom and *P* value noted *Give P values as exact values whenever suitable.*
☒	☐	For Bayesian analysis, information on the choice of priors and Markov chain Monte Carlo settings
☒	☐	For hierarchical and complex designs, identification of the appropriate level for tests and full reporting of outcomes
☒	☐	Estimates of effect sizes (e.g. Cohen's *d*, Pearson's *r*), indicating how they were calculated

Our web collection on statistics for biologists contains articles on many of the points above.

Software and code

Policy information about availability of computer code

Data collection	Bio-Rad chemiDoc Touch Imaging Software V1.2, ZEISS ZEN software 2.5, Leica LAS AF Lite
Data analysis	GraphPad Prism 9, Adobe Photoshop CC, ImageJ

For manuscripts utilizing custom algorithms or software that are central to the research but not yet described in published literature, software must be made available to editors and reviewers. We strongly encourage code deposition in a community repository (e.g. GitHub). See the Nature Portfolio guidelines for submitting code & software for further information.

Data

Policy information about availability of data

All manuscripts must include a data availability statement. This statement should provide the following information, where applicable:

- Accession codes, unique identifiers, or web links for publicly available datasets
- A description of any restrictions on data availability
- For clinical datasets or third party data, please ensure that the statement adheres to our policy

The raw Illumina reads generated from RNA-seq experiments were deposited at NCBI Sequence Read Archive (BioProject ID: PRJNA1139386).The authors declare that all data supporting the findings of this study are available within the article and its Supplementary Information files, or from the corresponding author upon reasonable request.

Research involving human participants, their data, or biological material

Policy information about studies with human participants or human data. See also policy information about sex, gender (identity/presentation), and sexual orientation and race, ethnicity and racism.

Reporting on sex and gender	N/A
Reporting on race, ethnicity, or other socially relevant groupings	N/A
Population characteristics	N/A
Recruitment	N/A
Ethics oversight	N/A

Note that full information on the approval of the study protocol must also be provided in the manuscript.

Field-specific reporting

Please select the one below that is the best fit for your research. If you are not sure, read the appropriate sections before making your selection.

☒ Life sciences ☐ Behavioural & social sciences ☐ Ecological, evolutionary & environmental sciences

For a reference copy of the document with all sections, see nature.com/documents/nr-reporting-summary-flat.pdf

Life sciences study design

All studies must disclose on these points even when the disclosure is negative.

Sample size	No statistical methods were used to predetermine samples or outcomes.
Data exclusions	Data were excluded when negative or positive controls were not working.
Replication	Sample numbers and the number of biological replicates for each experiment are indicated in figure legends or methods section above. Experiments were repeated independently at least three times.
Randomization	The Arabidopsis seeds/cells/seedlings with the same genetic backgroud were randomly placed in the culture with/without treatments.
Blinding	The investigators were blinded to group allocation during data collection and analysis.

Reporting for specific materials, systems and methods

We require information from authors about some types of materials, experimental systems and methods used in many studies. Here, indicate whether each material, system or method listed is relevant to your study. If you are not sure if a list item applies to your research, read the appropriate section before selecting a response.

Materials & experimental systems

n/a	Involved in the study
☐	☒ Antibodies
☐	☒ Eukaryotic cell lines
☒	☐ Palaeontology and archaeology
☒	☐ Animals and other organisms
☒	☐ Clinical data
☒	☐ Dual use research of concern
☐	☒ Plants

Methods

n/a	Involved in the study
☒	☐ ChIP-seq
☒	☐ Flow cytometry
☒	☐ MRI-based neuroimaging

Antibodies

Antibodies used	The VSR antibody were homemade. Additional primary antibodies used were anti-actin (Biodragon, B1051), anti-NBR1 (Agrisera, AS14 2805) anti-cFBPase (Agrisera, AS04 043), anti-Myc (ABclonal, AE070), anti-GFP (Biodragon, B1025), and anti-ATG8 (ABclonal, A22294) .

Validation

(1) anti-VSR. Validation data are available in "Tse, Y. C., et al. Identification of multivesicular bodies as prevacuolar compartments in Nicotiana tabacum BY-2 cells. Plant Cell 16, 672-693 (2004)."
(2) anti-actin (Biodragon, B1051), https://www.biodragon.cn/cn/goods/goodsView?GoodsId=12618&Catalog=
(3) anti-NBR1 (Agrisera, AS14 2805) . https://www.agrisera.com/en/artiklar/nbr1.html
(4) anti-cFBPase (Agrisera, AS04 043). Data are available in https://www.agrisera.com/en/artiklar/cfbpase-cytosolic-fructose-16-bisphosphatase-marker-for-cytoplasm.html
(5) anti-Myc (Santa Cruz, SC-789). Data are available in https://www.scbt.com/scbt/product/c-myc-antibody-a-14
(6) anti-GFP (Biodragon, B1025). https://www.biodragon.cn/cn/goods/goodsView?GoodsId=1757&Catalog=
(7) anti-ATG8 (ABclonal, A22294) . https://abclonal.com.cn/catalog/A22294

Eukaryotic cell lines

Policy information about cell lines and Sex and Gender in Research

Cell line source(s)	The Arabidopsis PSB-D suspension cell line is provided by Dirk Inzé (VIB).
Authentication	N.A.
Mycoplasma contamination	N.A.
Commonly misidentified lines (See ICLAC register)	N.A.

Plants

Seed stocks	The Arabidopsis (Arabidopsis thaliana) ecotype Col-0 T-DNA insertional mutant of vsr1-2 (GABI_503A05); vsr2 (SALK_082962); vsr4 (SALK_094467); vsr5 (SALK_044991); vsr6 (SAIL_338_H03); vsr7-3 (SAIL_1158_H09) and atg5 (SAIL_129_B07) were ordered and confirmed as described previously (Zouhar et al., 2010, Plant Journal). Arabidopsis vha-a2 vha-a3 (Krebs et al, 2010, PNAS), rpm1-3 (Grant et al, 1995, Science), rps2-101C (Mindrinos et al, 1994, Cell), and rps4 (Wirthmueller et al, 2007, Curr Biol) were described previously.
Novel plant genotypes	Double or triple mutants were generated by crossing and screened by genotyping PCR. To generate the transgenic plants, all of the plasmids were introduced into Agrobacterium tumefaciens strain GV3101 and transformed into WT or mutants by floral dip. Fluorescent tagged transgenic plants in WT or indicated mutants were generated by transgene or crossing.
Authentication	For phenotype analysis, 6 days old seedlings on plates or 24 days old plants on soil were observed and quantified. For fluorescent lines, we selected lines in which fluorescence segregated 3:1 in F2 populations, indicating a single insertion locus. All lines chosen were phenotypically indistinguishable from wild-type plants unless stated otherwise in the manuscript. T-DNA insertions of the mutant lines were verified by PCR using primers specific for the appropriate gene and the T-DNA borders.